2026

Geant4 simulation of radiation effect on semiconductor materials and hetero-junction field-effect transistor (HFET)

BOSTON UNIVERSITY

COLLEGE OF ENGINEERING

Thesis

GEANT4 SIMULATION OF RADIATION EFFECT ON SEMICONDUCTOR MATERIALS AND HETERO-JUNCTION FIELD-EFFECT TRANSISTOR (HFET)

by

YICONG HUANG

B.S., Virginia Tech, 2023

Submitted in partial fulfillment of the

requirements for the degree of

Master of Science

2026

Approved by

First Reader

Enrico Bellotti, PhD
Professor of Electrical and Computer Engineering
Professor of Materials Science and Engineering

Second Reader

Anna Swan, PhD
Associate Professor of Electrical and Computer Engineering
Associate Professor of Physics
Associate Professor of Materials Science and Engineering

Third Reader

Masahiko Matsubara, PhD
Research Assistant Professor of Electrical and Computer Engineering

Acknowledgments

First, I would like to express my sincere gratitude to my advisor, Professor Enrico Bellotti, for his patient guidance, clear direction, and consistent support throughout this research. His insightful suggestions and feedback have been invaluable to the completion of this thesis.

I am grateful to Professor Masahiko Matsubara for his assistance in setting up the simulation server and Synopsys Sentaurus TCAD.

I would also like to thank Professor Matteo Alasio for his help with Sentaurus TCAD and for his detailed explanations of its underlying mechanisms.

I would like to thank my thesis committee member, Professor Anna Swan, for her kindness and professionalism, as well as for her thoughtful feedback on my thesis writing.

Finally, I extend my appreciation to all members of the Computational Electronics Group for creating a supportive and encouraging research environment.

GEANT4 SIMULATION OF RADIATION EFFECT ON SEMICONDUCTOR MATERIALS AND HETERO-JUNCTION FIELD-EFFECT TRANSISTOR (HFET)

YICONG HUANG

ABSTRACT

Electronic systems operating in the space environment are constantly exposed to high-energy cosmic radiation, ranging from protons to heavy ions, which can deposit significant energy into semiconductor devices and trigger Single Event Effects (SEEs). As Gallium Nitride (GaN) Hetero-junction Field-Effect Transistors (HFETs) become increasingly critical and widely used for high-frequency and high-power applications, establishing a reliable methodology to predict their radiation hardness and failure mechanisms—such as Single Event Burnout (SEB)—is essential. The objective of this thesis is to develop a comprehensive simulation framework that integrates the Geant4 Monte Carlo toolkit with TCAD Sentaurus to accurately model the energy deposition process and its subsequent impact on device operation.

The methodology begins with Geant4 simulations of ion-matter interactions, confirming that stopping power increases with both the atomic number of the incident ion and the density of the target material. Subsequently, a Geant4 simulation of a GaN HFET structure is performed to extract a three-dimensional spatial energy deposition profile. These simulations reveal that high-energy ions generate branched tracks due to the significant travel distance of delta electrons, rendering simple linear-track assumptions insufficient for accurate modeling. To bridge the gap between particle physics and device simulation, the extracted energy-deposition data are converted into electron-hole pair generation rates and mapped into a modified 2D TCAD Sentaurus model. Transient simulations conducted

under varying bias conditions exhibit a characteristic double-peak behavior in the drain current following an ion strike. Crucially, the results demonstrate a strong dependence on the operating voltage: at lower drain voltages, the device recovers to its normal off-state (Single Event Transient), whereas at higher voltages, the current continues to rise, leading to potential permanent device failure (Single Event Burnout).

This research successfully establishes a multi-physics framework that validates the necessity of accounting for complex 3D energy deposition profiles when analyzing radiation effects in advanced semiconductor devices.

Contents

List of Figures

List of Abbreviations

2DEG	....	Two-Dimensional Electron Gas
AlGaN	....	Aluminum Gallium Nitride
CMOS	....	Complementary Metal-Oxide-Semiconductor
CNO	....	Carbon-Nitrogen-Oxygen
CSV	....	Comma-Separated Values
GaN	....	Gallium Nitride
GeV	....	Giga-electron volt
GPS	....	General Particle Source
HFET	....	Hetero-Junction Field-Effect Transistor
keV	....	Kilo-electron volt
LET	....	Linear Energy Transfer
MeV	....	Mega-electron volt
MSE	....	Material Science and Engineering
PeV	....	Peta-electron volt
SEB	....	Single Event Burnout
SEE	....	Single Event Effect
SEFI	....	Single Event Functional Interrupt
SEGR	....	Single Event Gate Rupture
SEL	....	Single Event Latchup
SET	....	Single Event Transient
SEU	....	Single Event Upset
TCAD	....	Technology Computer-Aided Design

Chapter 1

Introduction

The objective of this thesis is to develop a simulation methodology (framework) that accurately describes the energy deposition process as radiation interacts with semiconductor materials and devices, and impacts device operation behavior. In this chapter, I will provide an introduction to the types of radiation that are typically encountered, including their formation and energy ranges.

1.1 Cosmic Radiation

The universe is considered one of the most extreme environments humans have encountered. As shown in Figure 1.1, it is filled with high-energy particle radiations from the Sun and galactic sources. More importantly, technological systems operating in outer space are tolerating this radiation bombardment every second.

Cosmic radiation can be characterized into three types of ions: Hydrogen Ion (Protons), Helium Ion (Alpha particle), and Heavy Ion (Ions that have atomic number $Z > 2$).

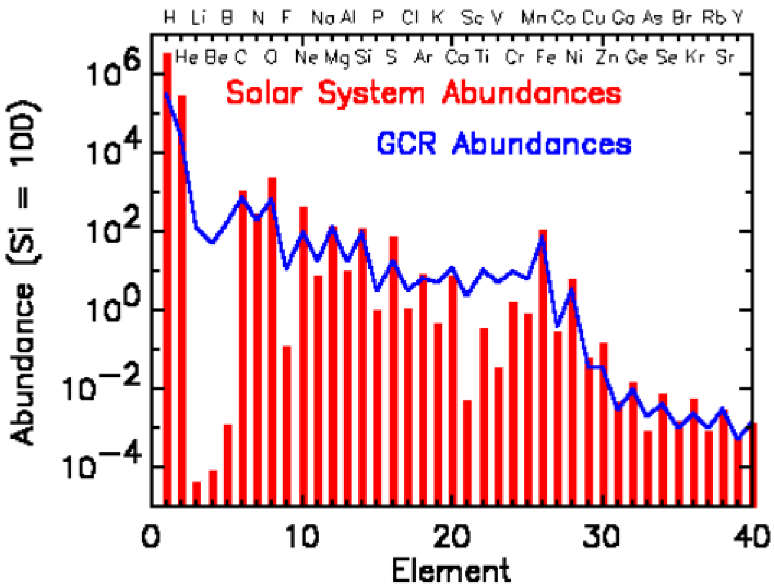

Figure 1·1: Element Abundance in the cosmic radiation (Whitman et al., 2019).

The plot provides a general overview of the elemental abundances in cosmic radiation originating from both the solar system and extragalactic sources. As shown, elements such as carbon, silicon, and iron are highly abundant in both radiation sources. This abundance is one of the reasons why these ions are selected as radiation sources in this study, as further described in the experimental setup.

A summary of how this ion is produced is shown in Figure 1.2. In addition, detailed information on these ions will be discussed in the following sections.

1.1.1 Protons (H^+ Ion)

The proton, or Hydrogen Ion (H^+), is the fundamental building unit of matter. It consists of three bound quarks (two up and one down), and these quarks combined together at the early stage of the Big Bang, formed protons and construct 75% of the material in the universe.(Elert, 1998). In today's universe, protons are being accelerated by solar activity and supernova explosions and become the most common type of space radiation. They contribute up to 95% (Coplan, 1995) of the radiation from the Sun and 85% (NASA, 2012) from the galactic sources, exhibiting a wide energy range from Mega-electron volt (MeV) to the Peta-electron volt (PeV) (Zhang et al., 2024a).

1.1.2 Alpha Particle (He^+ Ion)

The Alpha Particle, or Helium-4 nuclei, consists of two protons and two neutrons. They contribute approximately 23% of the material in the universe, and most of alpha particles are formed during the big bang shortly after the formation of protons through a two steps reaction process (Wright, 2012), where first proton (p) capture a neutron (n) to form a deuteron (d) and emit gamma ray (γ), then two deuteron (d) fuse together, forming Alpha Particle (^{4}He) and emit gamma ray (γ).

$$\mathrm{p} + \mathrm{n} \longrightarrow \mathrm{d} + \gamma$$
$$\mathrm{d} + \mathrm{d} \longrightarrow {}^4\mathrm{He} + \gamma$$

In the modern universe, new alpha particles continue to be produced inside stars primarily via the proton-proton (p-p) chain reaction (Kutner, 2003). It starts with the combination of two protons (^{1}H), forming a deuteron (^{2}H), emitting a positron (e^+) and a neutrino (ν). Then the deuteron captures a proton, forms a Helium-3 atom (^{3}He) and emits a gamma ray (γ). As the abundance of Helium-3 atoms reaches a certain level, they combine and form the alpha particle (^{4}He).

$${}^1\mathrm{H} + {}^1\mathrm{H} \longrightarrow {}^2\mathrm{H} + \mathrm{e}^+ + \nu$$
$${}^2\mathrm{H} + {}^1\mathrm{H} \longrightarrow {}^3\mathrm{He} + \gamma$$
$${}^3\mathrm{He} + {}^3\mathrm{He} \longrightarrow {}^4\mathrm{He} + {}^1\mathrm{H} + {}^1\mathrm{H}$$

Similar to the protons, alpha particle becomes a type of radiation after they are ejected from the inner layer of stars and accelerated through solar activity and supernova explosions. Alpha particle is the second abundant type of radiation, contributing 4% (Coplan, 1995) of the radiation from the Sun and 14% (NASA, 2012) from galactic sources, exhibiting an energy range from a few Mega-electron volt (MeV) per nucleus to Giga-electron volt (GeV) per nucleus (Naito & Kodaira, 2022).

1.1.3 Heavy Ion ($Z > 2$)

Heavy ion, in the context of radiation, refers to any ion with an atomic number(Z) greater than that of helium ($Z > 2$). All these elements are synthesized exclusively within stars.

CNO circle

For Carbon(C), Oxygen(O), and Nitrogen(N), which are the three most abundant heavy ions found in both solar radiation and cosmic radiation according to NASA's report (Whitman et al., 2019). They are synthesized via fusion processes called the CNO (Carbon-Nitrogen-Oxygen) cycle: (Wiescher, 2018)

$$
\begin{aligned}
{}^{12}\mathrm{C} + {}^{1}\mathrm{H} &\longrightarrow {}^{13}\mathrm{N} \\
{}^{13}\mathrm{N} &\longrightarrow {}^{13}\mathrm{C} + \beta^{+} \\
{}^{13}\mathrm{C} + {}^{1}\mathrm{H} &\longrightarrow {}^{14}\mathrm{N} \\
{}^{14}\mathrm{N} + {}^{1}\mathrm{H} &\longrightarrow {}^{15}\mathrm{O} \\
{}^{15}\mathrm{O} &\longrightarrow {}^{15}\mathrm{N} + \beta^{+} \\
{}^{15}\mathrm{N} + {}^{1}\mathrm{H} &\longrightarrow {}^{12}\mathrm{C} + {}^{4}\mathrm{He}
\end{aligned}
$$

The CNO cycle starts as a carbon-12 nucleus (${}^{12}C$) captures a proton (${}^{1}H$) and produce nitrogen-13 nucleus (${}^{13}N$). Due to the instability of nitrogen-13 nucleus, it emits a positron (β^{+}) and decays to carbon-13 nucleus (${}^{13}C$). Then the carbon-13 nucleus captures a proton and forms a nitrogen-14 nucleus (${}^{14}N$). Following the formation of the nitrogen-14 nucleus, it captures a proton and produces an oxygen-15 nucleus (${}^{15}O$). Similarly to the decay of nitrogen-13 nucleus, the oxygen-15 nucleus decays and forms a nitrogen-15 nucleus (^{15}N). At the end of the circle, the nitrogen-15 nucleus captures a proton, reproducing the carbon-12 nucleus and producing an alpha particle (^{4}He).

Helium Burning and Carbon Burning

As extra Helium is generated via the CNO cycle and hydrogen is exhausted, helium fusion begins. The process is called Helium burning, in which three helium nuclei fuse into one carbon nucleus (Salpeter, 1957):

$$^{4}\mathrm{He} + {}^{4}\mathrm{He} + {}^{4}\mathrm{He} \longrightarrow {}^{12}\mathrm{C}$$

Once the star exhausts helium, the core begins to contract, and the temperature rises. As the temperature rises sufficiently high enough, carbon starts to burn. This process is called carbon burning, and elements such as neon, sodium, and magnesium are synthesized through carbon fusion reactions. (Loore & Doom, 1992).

Neon Burning

After all the carbon is consumed, the star contracts further, resulting in a higher temperature, and neon starts to burn. During the neon burning process, more Oxygen and Magnesium are produced, forming a denser core at the end of the process, which leads to the next phase of the star's evolution - Oxygen burning (Loore & Doom, 1992).

Oxygen Burning and Silicon Burning

During the Oxygen Burning process, small amounts of Phosphorus and Sulfur, along with large amounts of Silicon, are produced by the dominant reaction (Meyer et al., 2008): $^{16}\mathrm{O} + {}^{16}\mathrm{O} \longrightarrow {}^{28}\mathrm{Si} + {}^{4}\mathrm{He}$. At the end of this process, a silicon core with extremely high temperature is formed, which leads to the Silicon-burning phase, ultimately resulting in the formation of Iron (Meyer et al., 2008).

Elements Beyond Iron

Elements that are heavier than Iron cannot be simply synthesized via "Iron Burning". Instead, they are produced by the following three processes:

- **r-process**: Rapid neutron capture process, also known as r-process, which is a phenomenon that occurs when the environment reaches a sufficiently high neutron density and temperature. Under these conditions, nuclei will rapidly capture neutrons to form progressively heavier nuclei. This process is one of the primary mechanisms for producing elements heavier than iron (Cowan et al., 2021).
- **s-process**: Slow neutron capture process, also known as s-process, which is a phenomenon that occurs at relatively low neutron densities, where the neutron capture times are much longer than typical β-decay half-lives. Under these conditions, the process will follow a certain path close to the valley of stability (Käppeler, 1999).
- **Proton-rich nucleosynthesis**: Proton-rich nucleosynthesis occurs primarily through two distinct mechanisms: the p-process and the rp-process. *p-process* is a phenomenon that occurs when the energy of a photon is sufficiently high and an abundance of protons. Such environments are typically created during a supernova explosion. In the process, energetic photons eject neutrons, protons, or alpha particles from nuclei (photodisintegration). *rp-process* occurs after the p-process, as resulting lighter nuclei may then capture protons and alpha particles, leading to the formation of heavier nuclei (Arnould & Goriely, 2003).

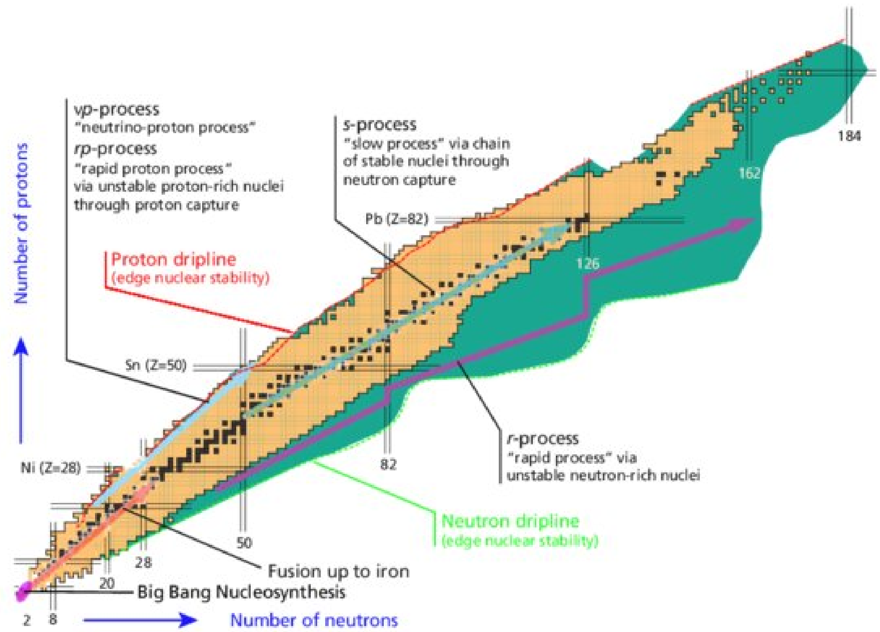

Figure 1·2: Summary of all the different nucleosynthesis paths (Rodríguez, 2014).

Similar to protons and alpha particles, these ions become a form of cosmic radiation after being ejected and accelerated by solar activity and supernova shockwaves. **These ions process a wide energy range, from kilo-electron volts (keV) per nucleon to Giga-electron volts (GeV) per nucleon** (Cohen et al., 2005).

Chapter 2

Physics Behind the Simulation

This chapter will discuss the physics theory that is included in the simulation, which consists of the physics of stopping interaction, the physics of semiconductor material and devices, and the physics of single-event effects.

2.1 Physics of Stopping Interaction

When high-energy particles enter a material, they interact with either the electrons or the nuclei. These interactions absorb the kinetic energy of the incident particles and prevent them from moving further; this process is called **stopping interaction**. There are two major types of stopping interaction: **electronic stopping interaction**, and **nuclear stopping interaction**. In this thesis, I will primarily focus on electronic stopping, since it dominates the energy-loss process in the MeV-GeV energy range (Sand et al., 2019).

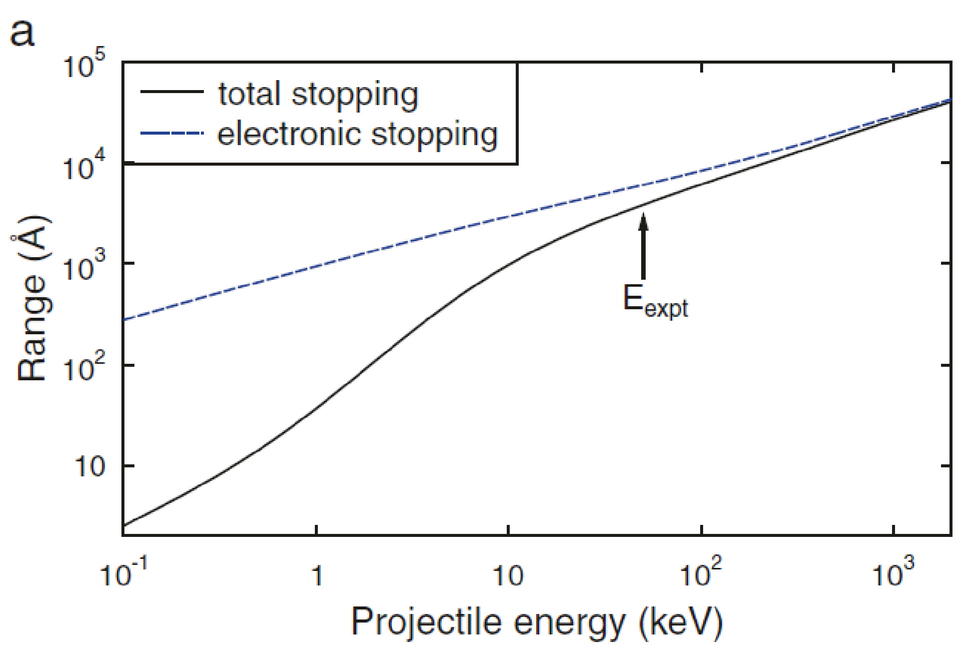

Figure 2·1: Relation of Electronic Stopping Power and the Total Stopping Power in the perspective of projectile energy (Sand et al., 2019).
This figure demonstrates that when the projectile energy lies within the MeV regime, such as the heavy-ion radiation discussed previously, the electronic stopping power is approximately equal to the total stopping power in terms of its influence on the projectile's penetration range in the material.

As shown in Figure 2.1, the electronic stopping and total stopping agree with each other when the projectile energy is above the 1 MeV range. However, in the low-energy regime, considering only the electronic stopping leads to an underestimation of the total stopping power, resulting in an overestimation of the penetration depth.

2.1.1 Electronic Stopping in Element Material

There are typically four mechanisms by which a charged particle loses energy through electronic interaction in materials (Quadros de Aguiar et al., 2024):

- **Ionization:** The incident charged particle deposits sufficient energy to an electron, causing the electron to escape from its host atom.

- **Excitation:** The incident charged particle transfers energy to the electrons, promoting them from a low-energy level to a high-energy level within the same atomic structure.

- **Elastic Collision:** The incident charged particle undergoes a change of its motion direction due to interaction with electrons, while its total kinetic energy is conserved.

- **Bremsstrahlung:** A Photon is emitted as a charged particle accelerated or decelerated after interacting with the electric field of the nuclei.

Ionization and Excitation are the two dominant mechanisms contributing to the stopping of incident charged particles in a solid, as elastic collisions do not cause any energy loss, and bremsstrahlung has an extremely low happening rate in heavy-ion-matter interaction.

2.1.2 Original Bethe–Bloch Formula

To better understand the electronic stopping problem, the Bethe–Bloch formula is investigated. The Bethe-Bloch formula describes the mean energy loss of a charged particle per unit distance — dE/dX, also known as stopping power. The first non-relativistic version was found by Hans Bethe in 1930, and the relativistic version was found by him in 1932 (Sigmund, 2006).

$$-\frac{dE}{dx} = \frac{4\pi e_1^2 e^2 Z_2 N}{mv^2} \sum_j f_{j0} \left[\ln\left(\frac{2mv^2}{\hbar\omega_{j0}}\right) - \ln\left(1 - \frac{v^2}{c^2}\right) - \frac{v^2}{c^2} \right].$$

This formula describes the energy loss per unit distance (dE/dX) of a charged particle with incident velocity v and charge number e_1 through a material. Here, c is the speed of light, e is the electron charge, m is the electron rest mass, Z_2 is the atomic number of target nucleus, N is the number density of atoms of the target material, f_{j0} is the dipole oscillator strength, which is the the probability of an electric dipole transition between two energy levels in an atom or molecule, and ω_{j0} is the transition frequencies.

2.1.3 Corrected Bethe–Bloch Formula

The Original Bethe-Bloch is most accurate when the target material is in the gaseous phase. Although its validity is limited across different materials and phases, it established an important foundation for the later development of a more general stopping power formulation. To address more complex problems, corrections are added to the original Bethe–Bloch formula, forming the modern version of it (Lindhard & Sørensen, 1996):

$$-\frac{dE}{dx} = \frac{4\pi Z_1^2 e^4}{mv^2} N Z_2 L.$$

Here, Z_1 is the atomic number of the incident particle, N is the number density of atoms in the target material, Z_2 is the atomic number of the target, m is the electron mass, and L is the stopping number. The stopping number includes the standard relativistic term and several higher-order corrections, and can be expressed as:

$$L = L_{\text{stand}} + \Delta L + \delta L_{\text{shell}} + \delta L_{\text{Barkas}} + \delta L_{\text{scr}},$$
$$L_{\text{stand}} = \ln\left(\frac{2mv^2}{I}\gamma^2\right) - \frac{v^2}{c^2} - \frac{1}{2}\delta,$$

with $\gamma = (1 - v^2/c^2)^{-1/2}$, and I is the mean ionization energy that can be calculated using Bethe's method: $Z_2 \ln I = \sum_j f_{j0} \ln\left(\hbar\left|\omega_{j0}\right|\right)$, where f_{j0} is the dipole oscillator strength, and ω_{j0} is the transition frequencies. In addition, all the higher-order corrections will be addressed by the following subsections, except for the L_{scr}, which is usually negligible.

2.1.4 $\mathbf{L_{\text{shell}}}$, Shell Correction

In the original Bethe's stopping power formula, it is assumed that the velocity of the incident particle is much larger than the orbital velocity of the bound electrons in the target atom. The Shell correction accounts for the situation that the velocity of the incident particle is comparable to the velocity of the bound electrons (Berger et al., 1993). It serves the purpose of connecting the high-velocity region and the low-velocity region of the stopping process. In addition, due to the fact that the Shell Correction will vanish on the high-velocity regime, for modern calculations the standard non-relativistic shell correction is considered accurate and is used: $\delta L_{\text{shell}} \approx -1.5 Z_2^{4/3}\ v_0^2/v^2$ (Lindhard & Sørensen, 1996).

2.1.5 δ, Density Effect Correction

Density Effect Correction addresses the decrease in stopping power caused by a specific physics phenomenon, known as the density effect. The density effect arises as a charged particle travels through a material, polarizing the medium. This polarization reduces the electromagnetic field acting on the incident particle, thereby reducing the energy loss of the incident particle. More importantly, the greater the particle velocity, the greater is the density effect (Berger et al., 1984). For modern simulation and calculation, a general numerical expression of the density effect correction is used (Sternheimer & Peierls, 1971), and is displayed in the Appendix A.

2.1.6 L_{Barkas}, Barkas Correction

The Barkas Correction is applied to address the Barkas-Andersen effect, which refers to two experimental observations that the original Bethe formula did not explain. First, Barkas observed that a negatively charged particle has a smaller stopping cross section than its equivalent antiparticle. Second, Andersen observed that the stopping power of a bare helium ion is four times higher than that of a bare proton, which violates the Z_1^2 dependence predicted by the original Bethe formula (Sigmund & Schinner, 2014). A modern approach to calculating Barkas correction is given by J. C. Ashley and R. H. Ritchie (Ashley et al., 1973):

$$L_{\text{Barkas}} = \frac{1.29F_A(b/x^{1/2})}{Z^{1/2}x^{3/2}},\ x = \frac{\beta^2}{Z\alpha^2},$$

where, $\alpha = 1/137.03604$, $\beta = v/c$, and F_A is a tabulated function (Appendix B).

2.1.7 ΔL, Bloch Correction and its Extension

Bloch correction acts as a bridge between the original Bethe's formula of stopping, which treats the electric field of the incident particles as a small perturbation on the target atom's electrons, and Bohr's classical theory, which treats the interaction as a classical Coulomb collision between two point charges (Sigmund & Schinner, 2020). Bloch correction can be expressed as the following (Berger et al., 1993):

$$z^2L_{\text{bloch}} = -y^2\sum_{n=1}^{\infty}\left[n(n^2+y^2)\right]^{-1},\ y = z\alpha/\beta,$$

where, z is the charge number of the projectile, α = 1/137.03604, and $\beta = v/c$. In this expression, for $y << 1$, the Bloch correction is negligible, and for $y >> 1$, the Bloch correction returns to the classical regime described by Bohr.

Lindhard-Sørensen Extension

Lindhard-Sørensen's extension is a complement to Bloch's correction. It extends Bloch's correction to the ultra-relativistic regime ($v \approx c$) by employing relativistic scattering kinematics and the Dirac equation. In addition, Lindhard-Sørensen incorporated both the Barkas correction and Bloch's correction to provide a more accurate approximation of heavy-ion stopping (ICRU, 2005).

2.1.8 Electronic Stopping Power in Compound

When calculating the electronic stopping power in a compound, using only the corrected Bethe–Bloch formula is not sufficient. To address this, Bragg's rule is applied. According to Bragg's rule, the stopping power of a compound can be approximated as the linear sum of the stopping powers of its constituent atoms, weighted by their fractional contribution to the compound's density(CERN, 2024).

2.2 Physics of Semiconductor

As mentioned earlier in the introduction section, semiconductor material and devices are the focus of this study. In this section, I will review the fundamental theory of semiconductor materials and devices. Having a basic understanding of semiconductor physics is essential for interpreting their behavior under radiation effects.

2.2.1 Energy Band Structure

In an isolated atom, electrons occupy distinct and discrete energy levels. All atoms of the same element have identical energy levels when they are far apart from each other. However, when these atoms come together to form a solid, the outermost electrons are influenced by the nuclei of all the surrounding atoms. This interaction causes their energy levels to shift and split into a series of closely spaced energy levels, which is known as the energy band structure (Kittel, 2004).

There are two band structures in a solid: **the valence band**, which lies at a lower energy level and electrons are packed with no free space to move; and the **conduction band**, which lies at a higher energy level, where electrons have the energy to freely travel through the material and contribute to the conductivity of the material. Between the valence and conduction bands, a region that may exist with no electron states, depending on the type of material, is known as the band gap. In addition, the magnitude of the gap determine the category of the materials as shown in Figure 2.2.

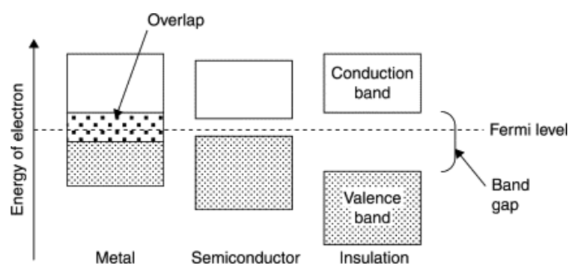

Figure 2·2: Band-gap in different types of material (Choudhury, 2014).

In semiconductors and insulators, the presence of a band gap causes electrons to stay bound in the valence band at room temperature, resulting in no electrical conductivity. Electrical conductivity only occurs as electrons in the valence band gain sufficient energy to be excited into the conduction band. For an insulator, the minimum energy required to promote an electron across the band gap is typically greater than 5 eV, whereas for a semiconductor, this energy is typically around 1 eV. In a conductor, the valence band and conduction band overlap ; therefore, no extra energy is needed to promote an electron. As a result, conductors exhibit electrical conductivity even at room temperature.

2.2.2 Charge Carriers and P-n Junction

As mentioned above, in a semiconductor, electrons need to gain sufficient energy to migrate from the valence band to the conduction band. When an electron crosses the band gap, it leaves a vacancy in its original position, known as a *hole*. Under the influence of an external electric field, electrons in the conduction band can move and form a current. At the same time, their corresponding holes in the valence band move in the opposite direction. Therefore, holes can be considered as positive charge carriers that also conduct the electric current. In summary, semiconductors have two types of charge carriers in total: electrons in the conduction band act as negative charge carriers, and holes in the valence band act as positive charge carriers. By contrast, due to the absence of a band gap, electrons are the only charge carrier in a conductor.

In a pure semiconductor, the number of holes is equal to the number of electrons. However, in practical applications, impurities, known as dopants, are intentionally introduced into the material to increase the charge-carrier concentration and improve conductivity. There are two types of dopant: p-type dopant, which introduces extra holes in the material, and n-type dopant, which creates extra electrons in the material. Semiconductors doped with p-type dopant are called p-type semiconductors, where holes are the majority carriers. Similarly, semiconductors doped with n-type dopant are called n-type semiconductors, where the electrons are the majority carriers.

p-n junction

When a p-type semiconductor and an n-type semiconductor are brought into contact, a special region forms at the interface, as shown in Figure 2.3, which is known as the p–n junction.

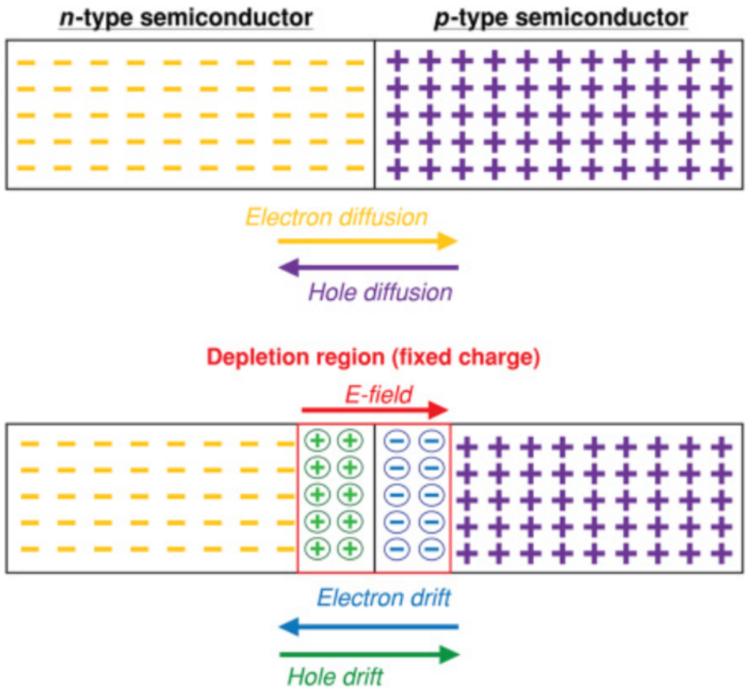

Figure 2·3: formation of *p*-*n* junction (Karaağaç et al., 2023).

This phenomenon occurs because the *n*-type semiconductor has a higher concentration of electrons, while the *p*-type semiconductor has a higher concentration of holes. As a result, holes from the *p*-side diffuse into the *n*-side, and electrons from the *n*-side diffuse into the *p*-side. During this diffusion process, immobile ionized atoms are on both sides of the junction. These charged ions create an internal electric field across the junction, which prevents further diffusion of carriers. The region depleted of free carriers is called the depletion region. At equilibrium, the rate of carrier diffusion is balanced by the rate of carrier drift caused by the electric field.

2.2.3 Hetero-junction

Besides the *p*-*n* junction, another important type of semiconductor junction commonly found in devices is the hetero-junction. Unlike a *p*-*n* junction, the formation of a hetero-junction does not require doping, but instead requires the interface of two different types of semiconductor with distinct properties, such as different band gaps or electron affinities. When these two semiconductors are brought together, their band structures will realign to achieve equilibrium, leading to the formation of an energy barrier or a potential well for electrons and holes. Similar to a *p*-*n* junction, the band realignment creates an internal electric field at the interface, as shown in Figure 2.4.

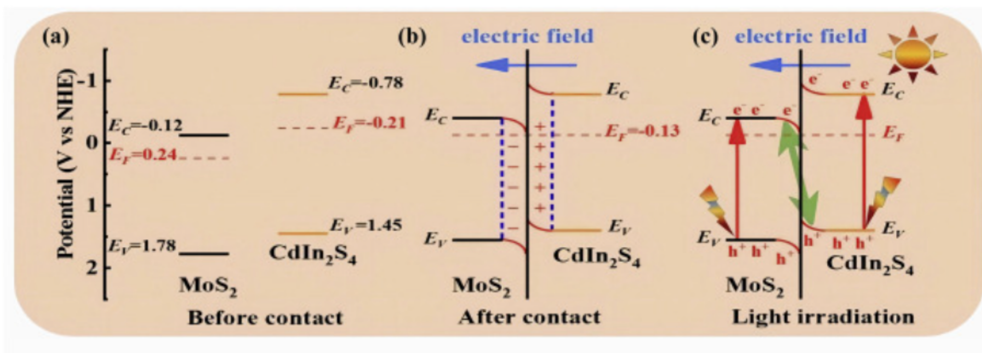

Figure 2.4: Formation of Hetero-junction (Lv et al., 2022).

AlGaN/GaN HFET

A classic example of a heterojunction structure is the AlGaN/GaN interface, which is widely used in Heterojunction Field-Effect Transistors (HFETs). Unlike a typical heterojunction where band offsets alone determine carrier confinement, the AlGaN/GaN system uniquely benefits from strong spontaneous and piezoelectric polarization inherent to III-nitride materials. More specifically, both AlGaN and GaN possess large spontaneous polarization, and the lattice mismatch that occurs when AlGaN is grown on GaN induces additional piezoelectric polarization in the strained AlGaN layer. The discontinuity of these polarization charges at the interface produces a substantial built-in electric field, which bends the conduction band and drives electrons toward the AlGaN/GaN interface. As electrons accumulate at this interface, they become confined in the resulting triangular quantum well, forming a high-density two-dimensional electron gas (2DEG), as shown in Figure 2.5 without the need for intentional doping.

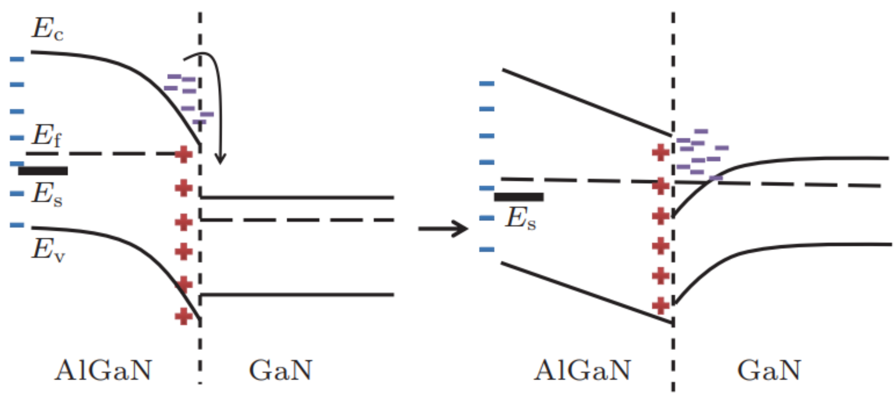

Figure 2·5: Formation of 2DEG at undoped AlGaN/GaN interface (He et al., 2015).

In an HFET, as shown in Figure 2.6, this 2DEG serves as the high-mobility channel between the source and drain terminals, enabling high current densities and electron velocities that are essential for high-frequency and high-power applications.

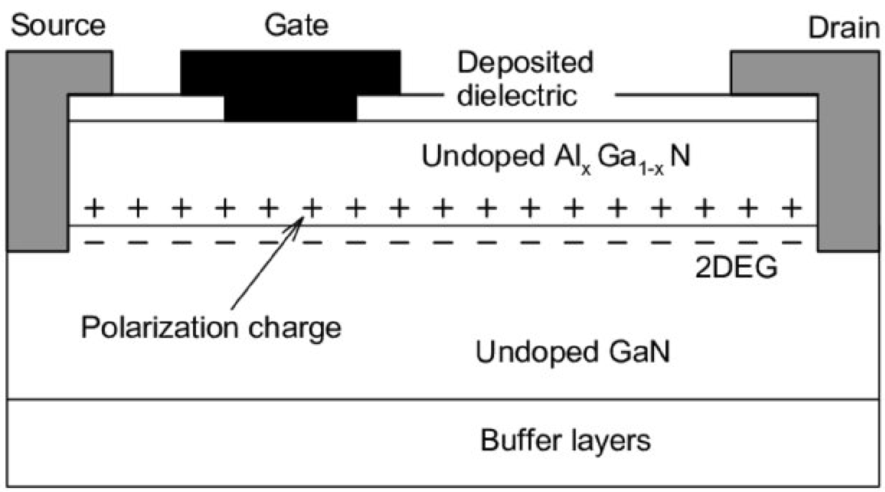

Figure 2·6: Cross section of a HFET (Dimitrijev et al., 2014)

2.3 Physics of Single Event Effect (SEE)

As discussed in the physics of Electronic Stopping, when a high-energy charged particle hits a material, it transfers its energy to the electrons. In addition, as noted in the theory of charge carrier in semiconductor, when an electron gains sufficient energy, it can cross the band gap and leave behind a hole. Consequently, in semiconductor materials and devices, this high-energy charged particle generates a dense track of electron-hole pairs along its path, as shown in Figure 2.7.

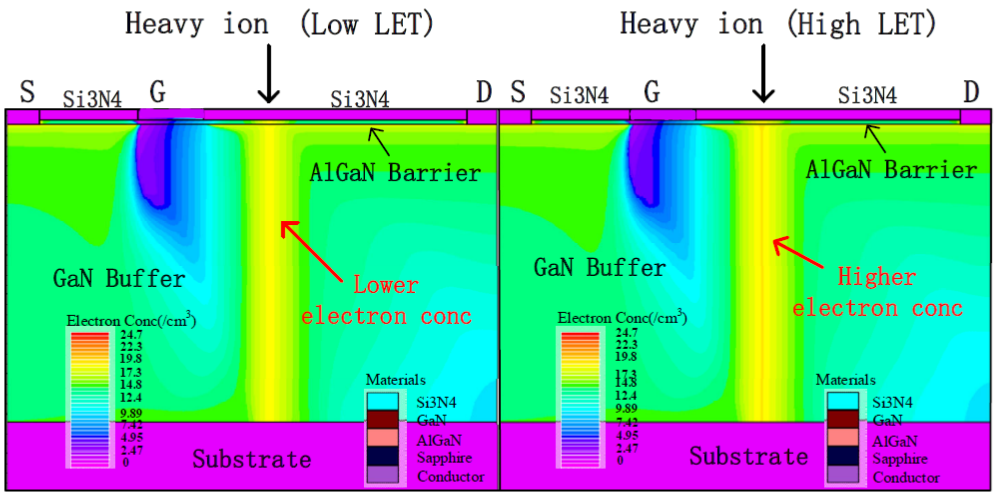

Figure 2·7: electron track along the path of the incident ion (Zhang et al., 2024b).

As showen in Figure 2.8, these electron–hole pairs are then transported under the influence of the device's electric field, holes are drifted towards the gate direction and electrons are collected by the drain. In addition, these charge carriers have a high chance to accumulate in a high electric field region, also known as a sensitive region, and cause device malfunction – such as a spike on the drain operation current, which later will be shown in example characterization plot of SEE.

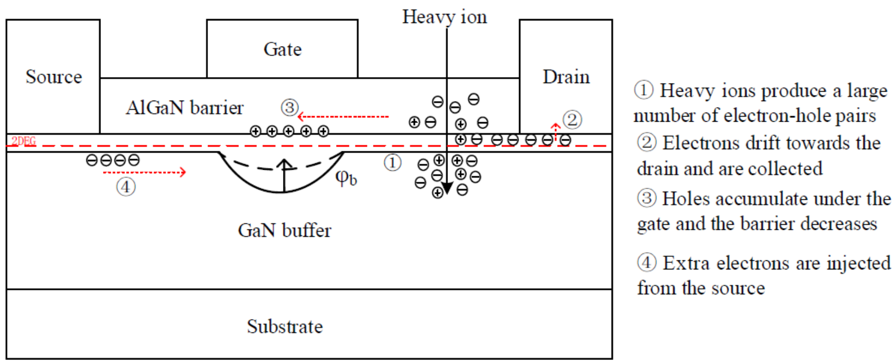

Figure 2·8: Charge carrier transportation in HFET(Zhang et al., 2024b).
The figure is a flow map of how the heavy-ion-induced charge carriers drift and diffuse in a HEFT under the influence of the HFET's electric field and how it impacts the HFET's operational behavior.

In summary, any malfunction in a device's operation caused by the impact of a single energetic particle is referred to as a Single Event Effect (SEE). In addition, SEE can be classified into two categories: non-destructive and destructive (FederalAviationAdministration, 2016):

Non-destructive SEE

Non-destructive SEE usually causes temporary device malfunction, and the device can recover either automatically or through manual intervention, such as a reboot. Several common non-destructive SEE examples will be listed here:

- **Single Event Upset (SEU)**: Charges generated by the incident charged particle can be collected by a nearby transistor, altering the state of a storage cell and leading to a soft error, commonly referred to as a bit flip.
- **Single Event Transient (SET)**: Charges generated by the incident charged particle create a short (transient) disturbance in the circuit, which can propagate through the circuit and potentially lead to a wrong logic state at the output.

- **Single Event Functional Interrupt (SEFI)**: In devices with complex state machines or control registers, charges generated by an incident charged particle can be collected by transistors, flipping the logical state of a critical bit and forcing the device into an unintended operation mode.

Destructive SEE

Destructive SEE is usually caused by the strike of a high-energy heavy ion on a highly sensitive region of the device, and the resulting damage is permanent. Several common destructive SEE examples will be listed here (FederalAviationAdministration, 2016):

- **Single Event Latchup (SEL)**: In CMOS technology, charges generated by the incident charged particles can trigger the parasitic bipolar (*p*-*n*-*p*-*n*) transistors, creating a low-impedance path from the power supply to ground. This causes a large, continuous current flow, which can lead to device overheating.

- **Single Event Burnout (SEB)**: In power transistors, charges generated by the incident charged particles can initiate a localized avalanche breakdown, particularly in regions with high electric fields. This breakdown can trigger a localized thermal runaway, leading to a permanent breakdown of the device.

- **Single Event Gate Rupture (SEGR)**: In power transistors, charges generated between the gate oxide and drain by the incident charged particle can create a transient electric field across the gate oxide. If this field exceeds the critical breakdown strength of the oxide, it induces a localized rupture, forming a conductive path between the device's conductive regions. This path increases the gate-leakage current, leading to device degradation and, ultimately, permanent failure.

2.4 Quantity in SEE Experiments: Mass Stopping Power vs Linear Energy Transfer (LET)

From the stopping power S (MeV/mm) discussed previously in the Bethe–Bloch formula section, an important quantity that is widely used in the radiation effect community — **the mass stopping power** S_m — is derived. S_m is defined as the stopping power divided by the material's density, giving it the unit of MeV·cm^2/mg, which makes this quantity independent of the material's phase.

Another important term that is commonly used in SEE experiments is the **Linear Energy Transfer** (LET, MeV·cm^2/mg). The terms S_m and LET are often confused because they have the same unit. However, these two quantities describe different physical aspects. Mass Stopping power describes how the ion loses energy as it interacts with the material, whereas Linear Energy Transfer describes how much of that energy is actually absorbed locally in the target material during the ion–matter interaction. Fundamentally, these two values are not equal, since the incident ion can transfer sufficient energy to an orbital electron, making it energetic enough to escape the orbital and travel some distance before interacting with the material and depositing its energy. These high-energy secondary electrons are called **delta electrons** or **delta rays**.

However, when the size of the target is much larger than the travel distance of the delta electrons, S_m and LET have the same value. In this scenario, all high-energy secondary electrons produced within the target are reabsorbed before escaping. Because the range of the secondary electrons is negligible compared to the target size, all of the energy transferred from the primary particle can be considered local.

2.5 Characterization of SEE

As discussed in the physics of SEE, the single-event effect causes abnormal behavior of the device's current. A way to characterize the occurrence of a single-event effect is to analyze how the change of devices' drain current (I_D) with respect to the operation time (t).

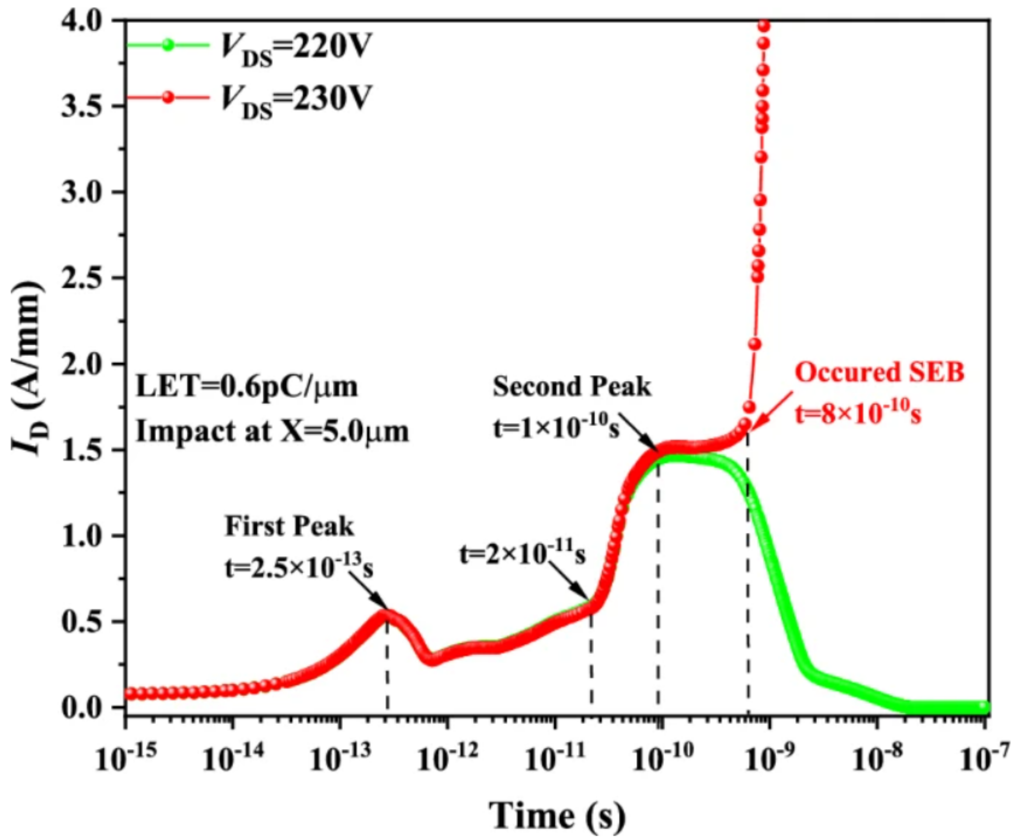

Figure 2·9: Sentaurus simulation result example of drain current versus operating time plot of heavy ion strike on a HFET (Li et al., 2025).

This figure demonstrates one way to characterize single-event effects (SEE): by analyzing the drain-current response over time following an ion strike. The red curve ($V_D = 230\,\text{V}$) shows a dramatic spike near the end of the transient, indicating the occurrence of a single-event burnout. In contrast, the green curve ($V_D = 220\,\text{V}$) shows that the drain current returns to its normal level, corresponding to a single-event transient.

Figure 2.9 is a classic characterization example of a single-event effect that happened on an HFET. In this example, a heavy ion with LET = 0.6 pC/μm strikes the drain-to-gate side of an off-state conventional HFET at $t = 10^{-13}$ s. Following the strike, a minor peak (the first peak) occurs at $t = 2 \times 10^{-13}$ s due to the increase of gate-to-drain leakage current caused by holes drifted from the shallower layers to the gate. Starting at $t = 2 \times 10^{-11}$ s, the drain current rapidly increases. This occurs because the holes generated in the buffer layer begin to accumulate beneath the gate, reducing the potential barrier between the source and the buffer layer, and creating an electron flux from the source to the buffer layer.

Starting from $t = 10^{-10}$ s, two potential outcomes could happen based on the operating voltage. When the bias is at V_{DS} = 220 V (green curve), the electrons injected from the source to the drain do not get sufficient energy to cause impact ionization, and eventually the drain current returns to the pre-radiation levels after a period of time. In contrast, when the bias is at V_{DS} = 230 V (red curve), these injected electrons from the source become highly energetic in the high-electric-field region between the drain and the gate, and cause local impact ionization, which generates more electron-hole pairs and causes further impact ionization and hole accumulation. As a result, the drain current increases dramatically and causes device destruction.

Chapter 3

Geant4 Simulation

As mentioned in the Introduction, the goal of this research is to develop a framework for radiation-effect simulation, and Geant4 constitutes the first component of this simulation framework.

This chapter addresses the Geant4 simulation of material and device behavior under the strike of high-energy heavy ions. Before presenting the experimental setup and results, I will first provide a detailed introduction to Geant4, including an overview of the toolkit, its simulation workflow, and an example simulation, to give the reader a clearer understanding of the software.

3.1 Geant4 Toolkit

Geant4 (Basaglia et al., 2024) is a free software toolkit developed in the C++ language and uses object-oriented technology to accurately simulate the passage of particles through matter. It has been widely used across many scientific fields, including particle physics, medical physics, nuclear physics, accelerator design, and space science. Generally speaking, when it comes to studying particle–matter interactions, Geant4 serves as a powerful simulation tool.

3.1.1 Introduction

Geant4 was originally developed to meet the need for a powerful detector simulation program with sufficient functionality and flexibility to support the next generation of subatomic physics experiments. Over time, it has evolved into a powerful tool capable of addressing a wide range of particle–matter interaction simulations. The spirit of Geant4 is its abundant set of physics models developed by researchers in the field of Monte Carlo simulation of physical processes.

The Geant4 toolkit has the following aspects of the simulation processes (S. Agostinelli, 2003):

- the geometry of the system,
- the materials involved,
- the fundamental particles of interest,
- the generation of primary events,
- the tracking of particles through materials and electromagnetic fields,
- the physics processes governing particle interactions,
- the response of sensitive detector components,
- the generation of event data,
- the storage of events and tracks,
- the visualization of the detector and particle trajectories, and
- the capture and analysis of simulation data at different levels of detail and refinement.

In Geant4, there are 17 class categories that cover all these aspects. A diagram demonstrating the classes and their relationships is shown in Figure 3.1.

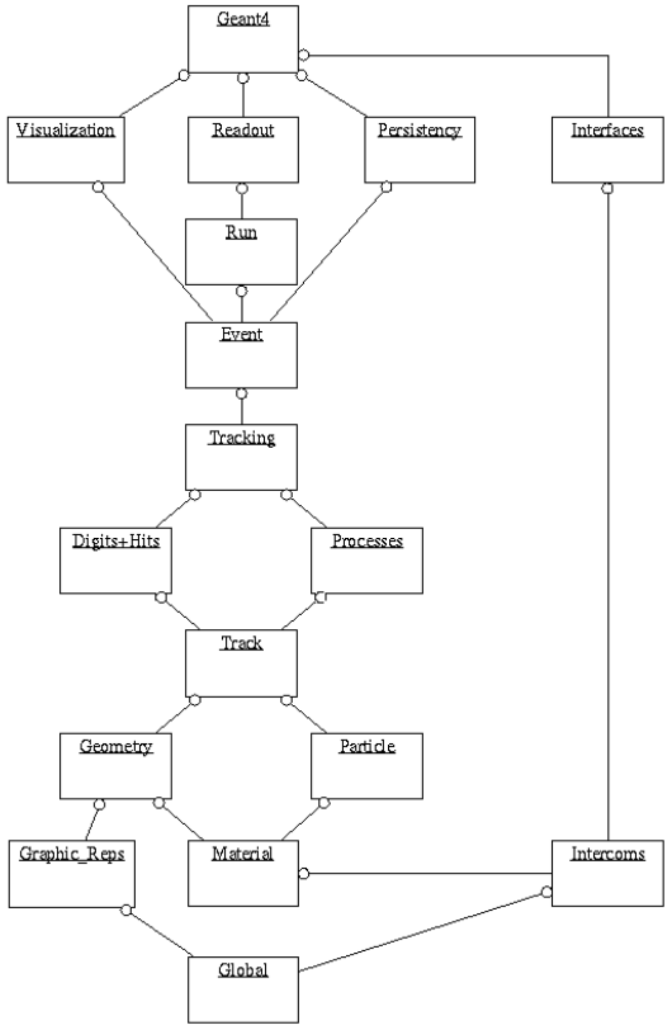

Figure 3·1: Geant4 class category (S. Agostinelli, 2003).
This plot is not a workflow chat of the Geant4 simulation software. Instead, it demonstrates the class categories and their relationships with each other: the category at the circle end uses the adjoining category. For example, both the Process and the Hits utilize the Track category, while they are independent of each other.

The boxes represent categories, meanwhile the open circle on the joining lines represents a using relationship, and the category at the circle end utilizes the adjoined category. In addition, Geant4 codes use this structure as a blueprint for construction.

There are a few important class categories that need to be illustrated in more detail (Yin, 2014):

- **Event**: The basic unit of a Geant4 simulation, which describes the entire process of a primary particle and its subsequent interactions, including the generation and transport of secondary particles as they propagate through the material geometry.
- **Track**: Represents a snapshot of a particle within an event, which records physical property information such as position, momentum, global time, and kinetic energy.
- **Step**: Steps provide incremental (Delta, Δ) information, such as energy deposition, time-of-flight by the step and propagation path within a track.
- **Run**: Represents the largest unit of the Geant4 simulation, which comprises the collection of all events that are generated under the identical condition.

3.1.2 Using Geant4

Geant4, as a toolkit, takes care of most of the aspects shown in Figure 3.1. In addition, a Geant4 flowchart is presented in Figure 3.2 to provide a clearer understanding of the process and illustrate how different classes are being utilized in the process.

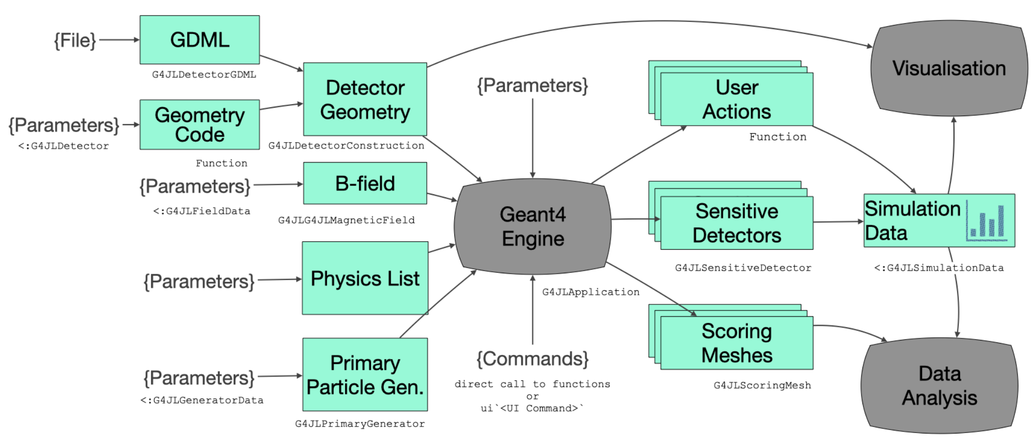

Figure 3·2: Geant4 simulation flowchart (JuliaHEP Collaboration, 2023).

From the flowchart, the whole process is categorized into two parts: **user initialization** and **user action**.

User initialization is the minimum requirement to run a Geant4 simulation, which includes constructing the detector geometry, magnetic field, physics list, and the generation of primary particles. To construct a detector geometry, the detector's dimensions and materials must be specified. To define a magnetic field, the field vector and its placement must be provided. To build a physics list, the relevant physics processes and simulation-related particles must be included. Finally, to generate primary particles, the particle type, energy, direction vector, and starting position must be addressed.

After the simulation, user actions can be performed, such as setting up a sensitive detector to study specific regions of the target by recording only that region's data. Data generated by the Geant4 simulation can also be exported into a comma-separated values (CSV) file for further analysis.

3.1.3 Geant4 Example

In this section, I will demonstrate a simple Geant4 simulation example of a 108 MeV silicon ion strike on a silicon slab, which is constructed based on the simulation flowchart.

Detector Construction

In Geant4, the target is treated as a detector. In the DetectorConstruction class, the cubic target detector is composed of the predefined Geant4 material – *G*4_*Si* and is constructed using the G4Box geometry method.

Physics List

The physics model used in this example is G4EmStandardPhysics_option4, and the electron cut value (the minimum kinetic energy allowed for delta electrons) is set to the lowest default value.

Primary Particle Generator

In this example, the incident ion is defined as a fully stripped 108 MeV silicon ion using the General Particle Source (GPS) method.

As discussed in Figure 3.2, these three classes are the essential components of the Geant4 simulation, and the result of this example is presented in Figure 3.3.

```
==== Primary Particle Info [Event 1] ====
G4WT0 >   Particle:  Si28
G4WT0 >   Energy:    108 MeV
G4WT0 >   Position:  0 0 -1.5 mm
G4WT0 >   Direction: (0,0,1)
G4WT0 >
====== Event -1 Track Details ======
G4WT0 > ==========================================
G4WT0 > [PRIMARY ION] Process=ionIoni Model=LindhardSorensen
G4WT0 > [PROCESS MODEL] At E=108 MeV: Using model: LindhardSorensen, dE/dx=16724.8 MeV/cm
G4WT0 > [PRIMARY] Depth=0.00 um, E/A=3.86 MeV/u, dE/dx=16724.76 MeV/cm (from process)
G4WT0 > [PRIMARY ION] Process=ionIoni Model=LindhardSorensen
G4WT0 > [PROCESS MODEL] At E=108.00 MeV: Using model: LindhardSorensen, dE/dx=16724.93 MeV/cm
G4WT0 > [PRIMARY] Depth=0.00 um, E/A=3.86 MeV/u, dE/dx=16724.93 MeV/cm (from process)
G4WT0 > [PRIMARY ION] Process=ionIoni Model=LindhardSorensen
G4WT0 > [PROCESS MODEL] At E=107.99 MeV: Using model: LindhardSorensen, dE/dx=16725.49 MeV/cm
G4WT0 > [PRIMARY] Depth=0.00 um, E/A=3.86 MeV/u, dE/dx=16725.49 MeV/cm (from process)
G4WT0 > [PRIMARY ION] Process=ionIoni Model=LindhardSorensen
G4WT0 > [PROCESS MODEL] At E=107.98 MeV: Using model: LindhardSorensen, dE/dx=16725.98 MeV/cm
G4WT0 > [PRIMARY] Depth=0.01 um, E/A=3.86 MeV/u, dE/dx=16725.98 MeV/cm (from process)
G4WT0 > [PRIMARY ION] Process=ionIoni Model=LindhardSorensen
G4WT0 > [PROCESS MODEL] At E=107.98 MeV: Using model: LindhardSorensen, dE/dx=16726.07 MeV/cm
G4WT0 > [PRIMARY] Depth=0.01 um, E/A=3.86 MeV/u, dE/dx=16726.07 MeV/cm (from process)
G4WT0 > [PROCESS MODEL] At E=107.98 MeV: Using model: LindhardSorensen, dE/dx=16726.15 MeV/cm
G4WT0 > [PRIMARY] Depth=0.01 um, E/A=3.86 MeV/u, dE/dx=16726.15 MeV/cm (from process)
G4WT0 > [PROCESS MODEL] At E=107.97 MeV: Using model: LindhardSorensen, dE/dx=16726.68 MeV/cm
G4WT0 > [PRIMARY] Depth=0.02 um, E/A=3.86 MeV/u, dE/dx=16726.68 MeV/cm (from process)
G4WT0 > [PROCESS MODEL] At E=107.97 MeV: Using model: LindhardSorensen, dE/dx=16727.37 MeV/cm
G4WT0 > [PRIMARY] Depth=0.02 um, E/A=3.86 MeV/u, dE/dx=16727.37 MeV/cm (from process)
G4WT0 > [PROCESS MODEL] At E=107.96 MeV: Using model: LindhardSorensen, dE/dx=16727.46 MeV/cm
G4WT0 > [PRIMARY] Depth=0.02 um, E/A=3.86 MeV/u, dE/dx=16727.46 MeV/cm (from process)
G4WT0 > [PROCESS MODEL] At E=107.96 MeV: Using model: LindhardSorensen, dE/dx=16727.95 MeV/cm
G4WT0 > [PRIMARY] Depth=0.02 um, E/A=3.86 MeV/u, dE/dx=16727.95 MeV/cm (from process)
G4WT0 > [DELTA-RAY e-] Process=eIoni Model=PenIoni E=0.99 keV
G4WT0 > [DELTA-RAY e-] Process=eIoni Model=PenIoni E=1.01 keV
G4WT0 > [DELTA-RAY e-] Process=eIoni Model=PenIoni E=1.01 keV
G4WT0 > [DELTA-RAY e-] Process=eIoni Model=PenIoni E=1.01 keV
G4WT0 > [DELTA-RAY e-] Process=eIoni Model=PenIoni E=0.99 keV
G4WT0 > [DELTA-RAY e-] Process=msc Model=Unknown E=1.01 keV
G4WT0 > [DELTA-RAY e-] Process=eIoni Model=PenIoni E=0.92 keV
G4WT0 > [DELTA-RAY e-] Process=eIoni Model=PenIoni E=1.00 keV
G4WT0 > [DELTA-RAY e-] Process=eIoni Model=PenIoni E=1.01 keV
G4WT0 > [DELTA-RAY e-] Process=eIoni Model=PenIoni E=1.03 keV
G4WT0 > [PHOTON HIT ADDED] #1 TrackID=10360 Edep=0.10 keV
```

Figure 3·3: Example of Geant4 simulation result.
This example result is displayed in the terminal and demonstrates the information included: incident ion, secondary electrons (delta electrons), interaction process (ion-ionization), used physics model (Lindhard-Sørensen), and the stopping power (dE/dX).

3.2 Geant4 Simulation of Radiation Energy Deposition in Materials

The Geant4 simulation of energy deposition in materials serves two main purposes. First, it helps establish a comprehensive understanding of how ions deposit energy when interacting with the target material. Second, the simulation results can be compared with published literature to validate the accuracy of the developed code.

In general, two types of simulation experiments are conducted for both the Si and GaN targets: the ion-energy comparison experiment and the ion-type comparison experiment. In this section, I will first describe the simulation setup in detail and then present the corresponding results.

3.2.1 Simulation Setup

In the simulation setup, the Geant4 class category and the Geant4 simulation process are followed closely. In this subsection, I will demonstrate both the user initialization component and the user action component of my setup.

User Initialization: Detector Construction

In the detector construction process, the outer environment where the target is set to be located in a vacuum, using the predefined Geant4 material – G4_Galactic. Then, the silicon target is constructed using the G4Box method and the predefined Geant4 material – G4_Si. The dimensions of the silicon box are set to be 10μm (width) $\times$ 10μm (height) $\times$ 800μm (long). This size ensures that the silicon target is large enough to accommodate variations in penetration depth during the ion energy comparison experiments and to minimize the effect of escaping delta electrons, so that the mass stopping power can be considered approximately equal to the linear energy transfer, as discussed in the S_M versus LET section.

The gallium nitride (GaN) target is constructed using the G4Box method and assigned the same dimensions as the silicon box. Because Geant4 does not include a predefined material for GaN, the material is manually defined by specifying a density of 6.15 g/cm^3, and composing it from one gallium atom and one nitrogen atom.

User Initialization: Primary Particle Generation

In the Primary Particle Generation class, the G4 General Particle Source (GPS) method is being used to construct the radiation source. This method allows users to modify the particle source by changing the parameters in the macro file instead of changing the code.

```
# ============================
# Primary Particle Source (GPS)
# ============================
/gps/particle ion
/gps/ion 14 28 14        # Si-28 ion
/gps/position 0 0 -1500 um
/gps/direction 0 0 1
/gps/energy 56 MeV
```

Figure 3·4: Example of a marco file.

For the ion energy comparison experiment, the incident ion is set to be a fully ionized silicon-28 ion with different energies: 2 MeV/n, 4 MeV/n, 6 MeV/n, 8 MeV/n, and 10 MeV/n, and located at (0,0,$-1500\,\mu$m), traveling in the positive z direction.

For the ion type comparison experiment, carbon-12 ion, neon-20 ion, silicon-28 ion, argon-40 ion, and Iron-56 ion are chosen as our incident ions, and the energy of all incident ions is set to be 10 MeV/n, with starting location at (0,0,$-1500\,\mu$m) and traveling in the positive z direction.

User Initialization: Physics List

To address the scenario of materials being struck by heavy ions with energies ranging from 2 MeV/n to 10 MeV/n, G4IonPhysics and G4EmStandardPhysics_option4 are chosen to construct the physics list. In this physics list, G4IonPhysics addresses potential nuclear elastic and inelastic interactions.

The G4EmStandardPhysics_opiton4 utilizes the G4Lindhard-Sorensen model for ion-matter interactions with energy greater 2 MeV/n, and the G4Lindhard-sorensen model is based on the corrected Bethe–Bloch formula that is discussed previously.

In addition, to fully utilize the delta-electron generation feature that Geant4 has, the electron energy cut is set to the lowest default value.

User Action

To record simulation data, the entire silicon and GaN targets are defined as sensitive detectors using the sensitive volume method. This ensures that every ion–matter interaction (hit) occurring within these volumes is recorded by the Geant4 engine. Data on the positions, kinetic energies of ions and delta electrons, as well as the ions' deposited energy and stopping power, were extracted into comma-separated values (CSV) files for further analysis. Moreover, according to the Monte Carlo statistical rule applied in Geant4, the statistical uncertainty is approximately $1/\sqrt{N}$, where N is the number of events. Therefore, all simulations were run with 200 events to maintain the uncertainty at about 7%.

3.2.2 Material Simulation Result

Besides extracting raw data from the experiment, as mentioned in the User Action section of the setup, an energy-deposition-versus-depth profile for both materials is constructed using MATLAB. This profile was generated from stopping-power and penetration-depth data obtained from the simulation.

Result and Code validation

After obtaining the energy-deposition-versus-depth profile, the Geant4 results are compared with SRIM simulation plots reported in an academic paper.

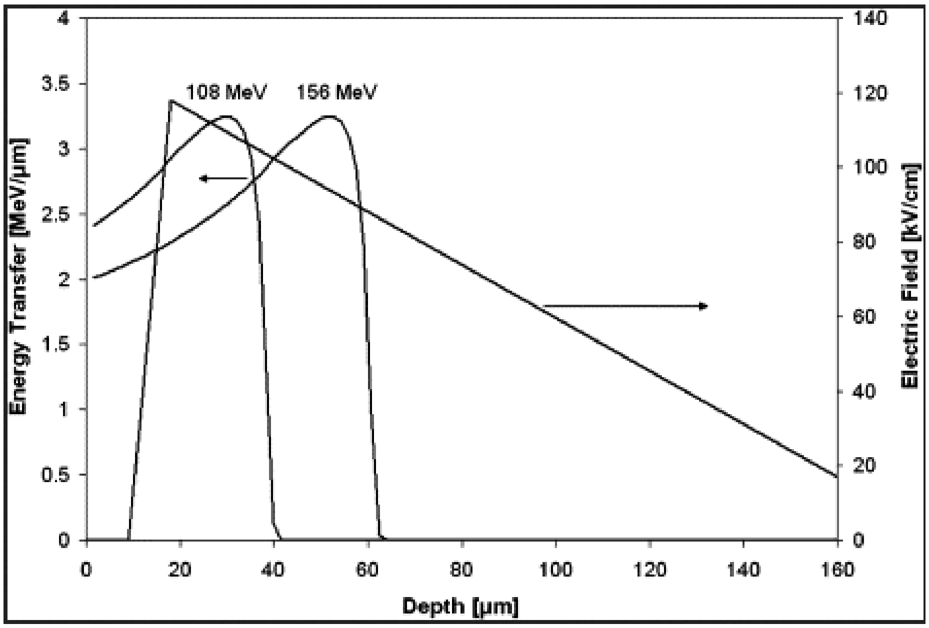

Figure 3·5: SRIM simulation of Si ion passing through a Si target, (Albadri et al., 2006).

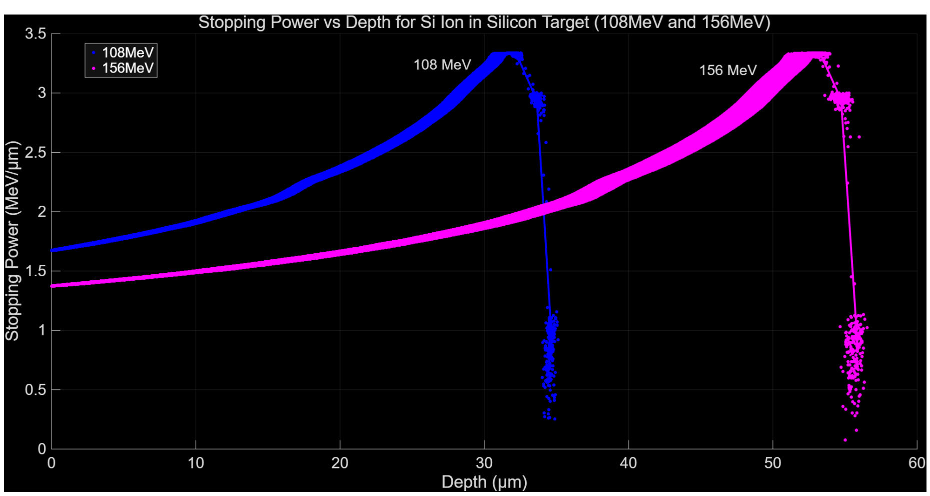

Figure 3·6: Stopping Power vs Depth of Si ion in Si Material.

By comparing these two results, two key features are observed that can confirm the validity of the Geant4 simulation results and code. First, the peak value is consistent: the maximum stopping power in the stopping-power-versus-depth profile matches that reported in the SRIM results. Second, the overall trends are similar—both plots show an increase in stopping power with depth, and the peak value remains unchanged as the depth varies.

Ion Energy Comparison Experiment Result and Discussion

Figures 3.7 and Figure 3.8 are the stopping power-depth profile of the ion energy comparison experiment, with ion penetration depth as the x-axis in the unit of μm and stopping power as the y-axis in the unit of MeV$/\mu$m.

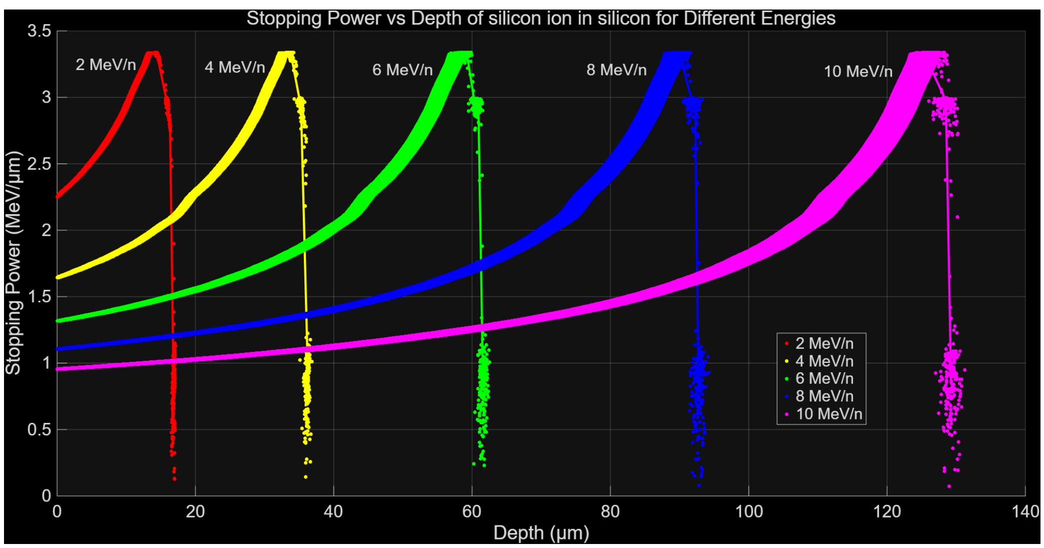

Figure 3·7: Stopping Power vs Depth of Si ion with different energies in Si Material

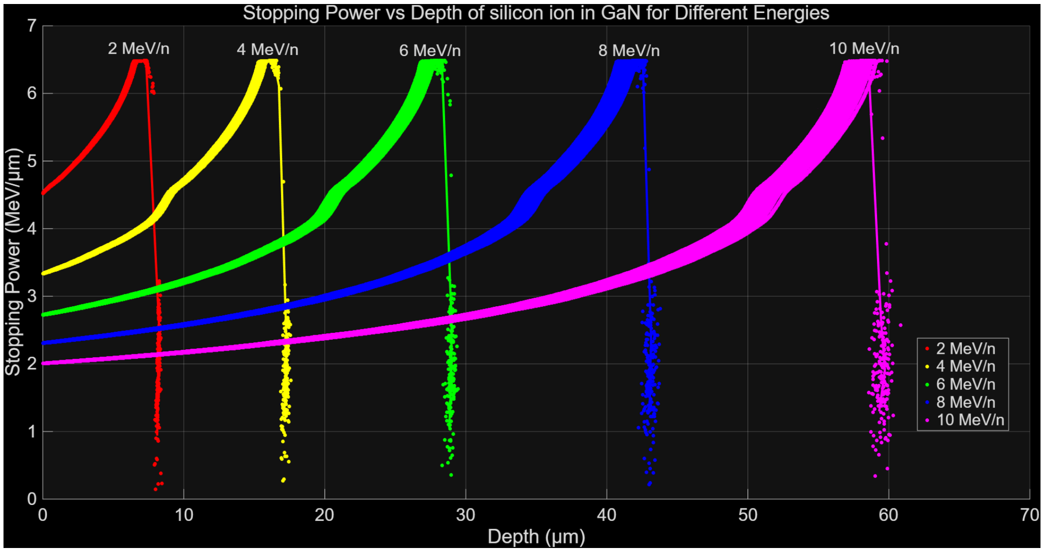

Figure 3·8: Stopping Power vs Depth of Si ion with different energies in GaN Material

As shown on the plots, there are three characteristics shown on each curve. First, as the ion progresses deeper in the material, the stopping power increases. Second, when comparing different curves, the incident stopping power decreases as the kinetic energy of the ion increases.

These two phenomena are both consequences of the ion's energy deposition. As the incident ion transfers its energy to the material, its velocity (v) decreases. From a mathematical perspective, both phenomena can be explained by the Bethe-Bloch formula, which indicates that stopping power has an inverse dependence on velocity (i.e., $dE/dx \propto 1/v^2$). From a physical perspective, when the ion moves more slowly, the interaction time with the target electrons becomes longer, allowing more energy to be transferred to the medium. As a result, the stopping power increases as the ion's velocity decreases.

More importantly, when comparing the Bragg peak values for different curves in the same material, it is observed that as the incident ion energy increases, only the position of the Bragg peak shifts deeper into the material, while the magnitude of the peak remains unchanged. This behavior can be explained by the definition of the Bragg peak: it corresponds to the point at which the ion deposits the maximum amount of its energy. When this definition is viewed in the context of the Bethe–Bloch formula, it becomes clear that the velocity at which this maximum energy deposition occurs is unique. Therefore, increasing the kinetic energy of the ion simply extends the distance required for the ion to decelerate to that characteristic velocity, thereby pushing the Bragg peak deeper into the material without changing its value.

Ion Type Comparison Experiment Result and Discussion

Figure 3.9 and Figure 3.10 are the stopping power-depth profile of the ion energy comparison experiment, with ion penetration depth as the x-axis in the unit of μm and stopping power as the y-axis in the unit of MeV$/\mu$m.

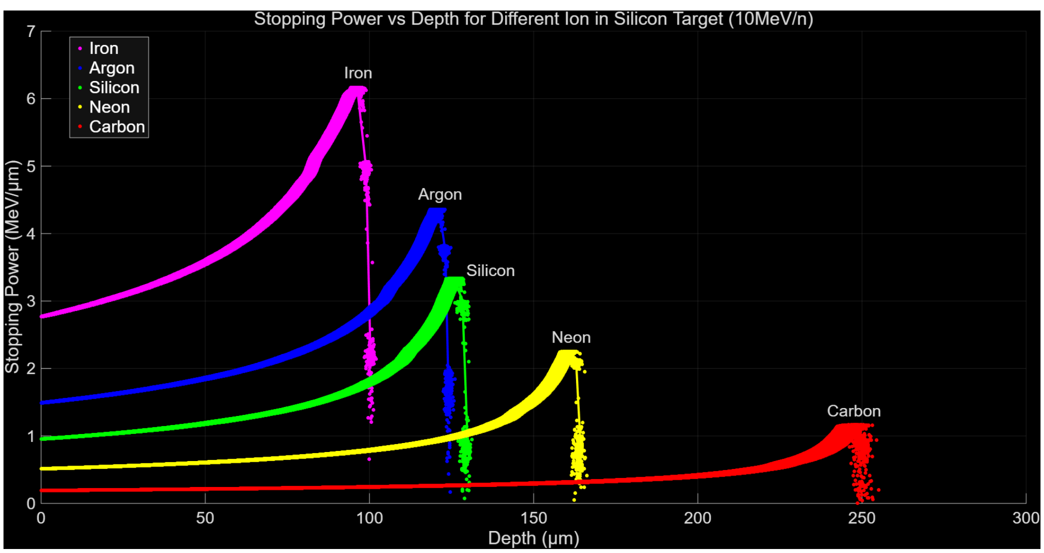

Figure 3·9: Stopping Power vs Depth of C, Ne, Ar, Si, and Fe ions in Si Material.

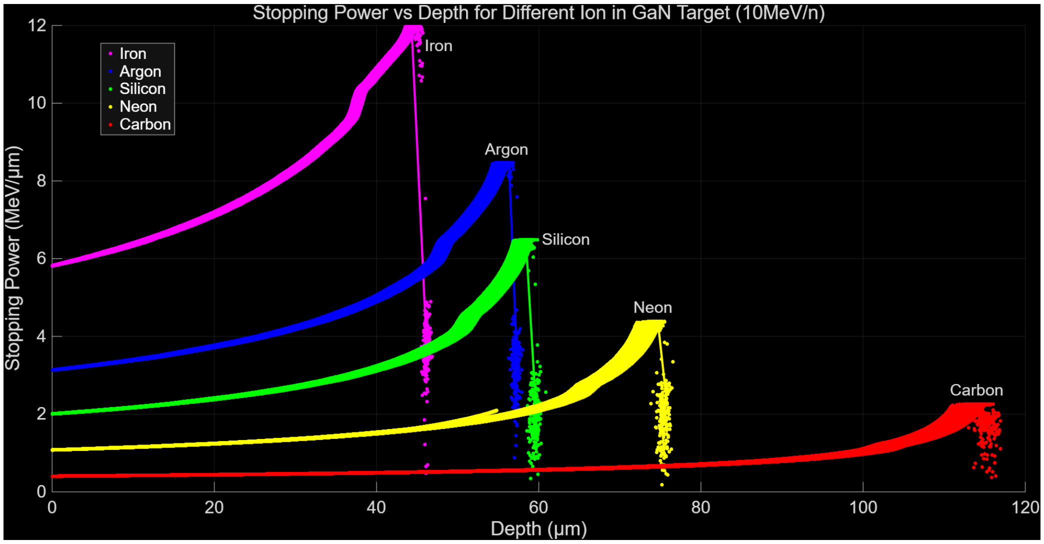

Figure 3·10: Stopping Power vs Depth of C, Ne, Ar, Si, and Fe ions in GaN Material.

The comparison of the Bragg curves for different ions in the same material shows that the stopping power increases with the atomic number of the incident ion.

From a mathematical perspective, based on the Bethe–Bloch formula, the stopping power is proportional to the square of the atomic number of the incident ion ($dE/dx \propto {Z_1}^2$). This means that ions with higher charge lose energy more rapidly as they travel through the material. From a physical perspective, a higher atomic number corresponds to a greater ion charge, which produces a stronger Coulomb interaction with the target electrons. This enhances both the probability and strength of ionization and excitation events. As a result, heavier ions deposit more energy per unit path length, leading to a higher stopping power.

This phenomenon also explains why heavier ions cause more damage to devices than lighter ions. Since heavier incident ions have stronger and more frequent electronic interactions with the device material, they generate a much larger density of electron–hole pairs along their track. This higher charge deposition increases the chance of disrupting the device's operation, especially in sensitive regions, thereby leading to a greater probability of single-event malfunction.

Further Analysis: Material Comparison and Discussion

After obtaining simulation results from both the silicon target and GaN target, a comparison between these two types of material is conducted to study how different materials will influence the stopping power.

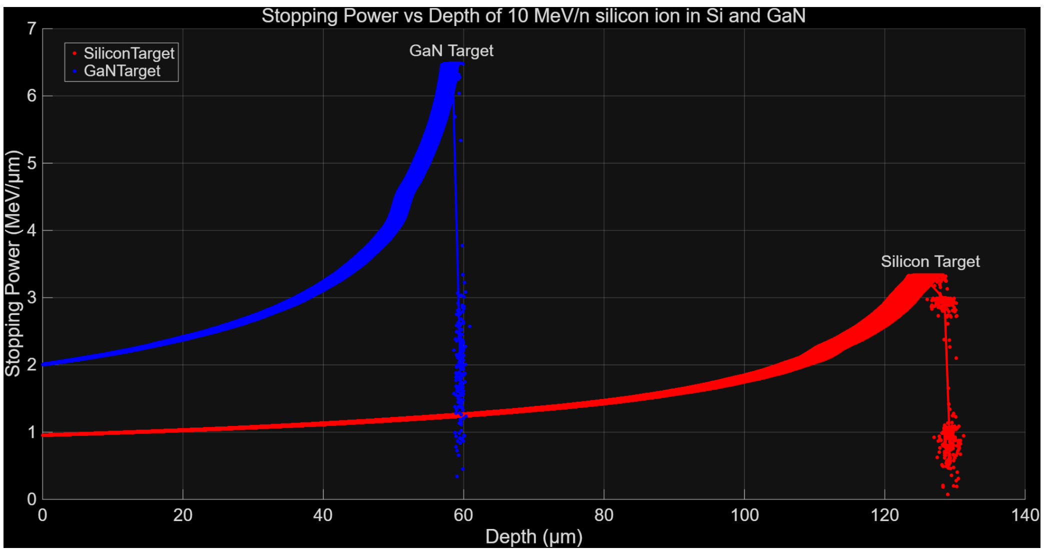

Figure 3·11: Stopping Power vs Depth of 10 MeV/n Si ion in Si and GaN Material.

As shown in Figure 3.11, the penetration depth of a 10 MeV/n Si ion in GaN is significantly shorter than that in Silicon. From a mathematical perspective, GaN has a larger atomic number (Z_2) and larger number density of atoms (N) than Si. Since stopping power is proportional to both Z_2 and N, an increase in these parameters results in a higher stopping power. Consequently, the Si ion loses energy more rapidly in GaN, leading to a shorter penetration depth.

From a physical perspective, GaN is more densely packed than Si, meaning that as the ion travels through the material, its electronic interactions occur more frequently and more strongly in GaN than in Si. This enhanced interaction increases the stopping power and therefore further reduces the ion's penetration depth.

3.3 Geant4 Radiation Effect Simulation in HFET Device

In this section, I will present the radiation-effect simulation work conducted on the HFET device. This includes setting up the Geant4 simulation to model ion–device interactions and performing post-processing of the resulting data for further analysis and device-level simulation.

3.3.1 Geant4 Simulation Setup of Radiation Effect in HFET Device

The Geant4 simulation setup for the HFET device is similar to that for material simulations. In this section, I will briefly go over the unchanged parts and elaborate on the changes, such as the detector structure, in detail.

Physics List

The physics list used in the device simulation is the same as that used in the material simulation.

Detector (HFET) Construction

The HFET structure used in the simulation is built based on the conventional HFET structure provided by the Sentaurus example – HFET_GaN_DC.

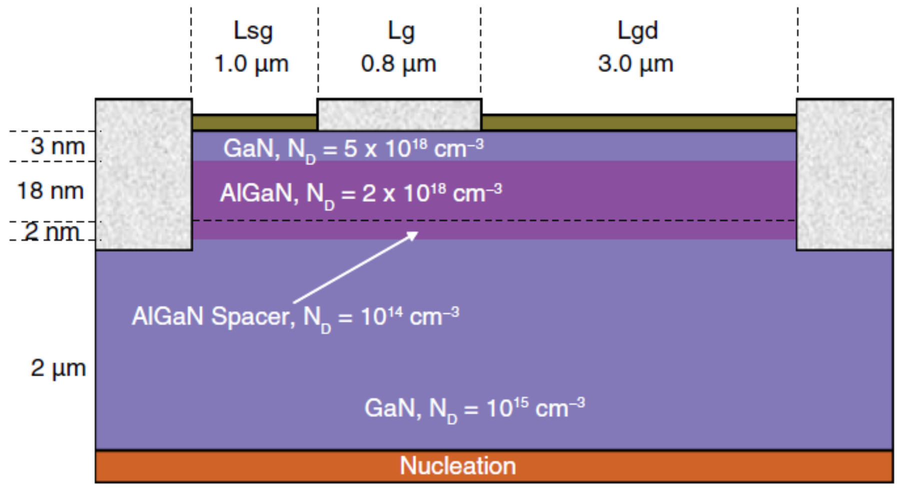

Figure 3·12: HFET Structure From Sentaurus Example.

The target structure used in the Geant4 simulation was modified based on the device structure shown in Figure 3.12. Since the absence of source and drain contacts, as well as the exclusion of doping profiles, does not significantly affect the ion energy deposition in the device, these features were not included in the Geant4 geometry.

Primary Particle Generation

The device simulation uses the same particle generation method (GPS) as the material simulation. In this simulation, the primary particle is set to be a 10 MeV/n fully ionized carbon ion traveling in the negative Z-direction and striking the HFET device at $Y = 3.8\,\mu$m.

3.3.2 Geant4 Simulation Result and Discussion of the HFET Structure

Simulation result is presented in the Figure 3.13.

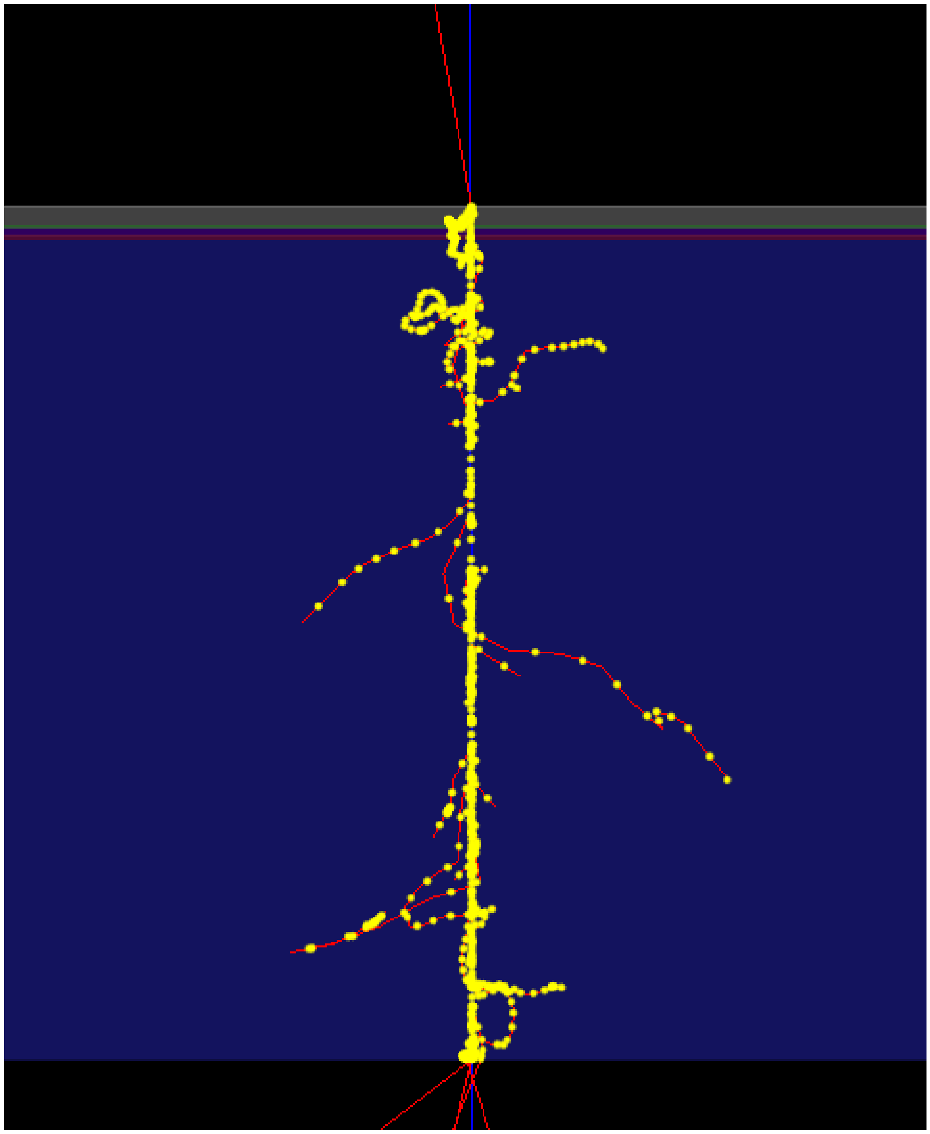

Figure 3·13: Geant4 simulation on HFET structure.
This figure visualizes a 10 MeV/n carbon-ion strike on an HFET structure. The ion trajectory, shown by the blue line, enters from the top, fully penetrates the device, and exits at the bottom. Each yellow point represents an interaction event along the ion's path, while the red segments connecting some of these points indicate interactions caused by secondary (delta) electrons.

From Figure 3.13, two key observations can be made. First, the carbon ion fully penetrates the device. Second, the energy deposition track is branched rather than forming a straight line, and delta electrons are generated during the ionization process. In addition, compared with the device dimensions, the travel distance of these delta electrons is not negligible. Therefore, describing the resulting charge distribution simply as a dense track along the ion path is not valid in this case. To accurately describe the charge distribution, spatial coordinates (X, Y, Z) and the corresponding deposited energy are extracted into a CSV file, and a three-dimensional spatial energy deposition profile is constructed using MATLAB.

A	B	C	D	E	F	G	H	I
TrackID	ParticleName	LayerName	X_nm	Y_nm	Z_nm	Depth_um	Time_ns	Edep_keV
Number	Number	Categorical	Number	Number	Number	Number	Number	Number
1	C12	Buffer	903.331	-0.22342	38.513	2.0345	0.00034344	0.00070009
1	C12	Buffer	903.334	-0.22561	36.2831	2.0367	0.00034349	0.00072468
1	C12	Buffer	903.343	-0.23386	27.5021	2.0455	0.00034385	1.0387
1	C12	Buffer	903.362	-0.24822	10.3755	2.0626	0.00034428	10.0224
1	C12	Buffer	903.374	-0.25575	0.48289	2.0725	0.0003443	0.00029815
2	e-	Cap	861.752	-66.1368	2022.13	0.050873	0.00029885	0
2	e-	Cap	862.219	-70.6234	2020.87	0.052129	0.00029895	0
2	e-	Cap	871.256	-73.4806	2020.71	0.052289	0.0002993	0.7497
2	e-	Cap	878.86	-74.6805	2021.1	0.051898	0.00029932	0.0070447
2	e-	Cap	879.97	-73.9745	2022.13	0.050865	0.00029939	0
4	e-	Buffer	908.21	1.6921	1974.11	0.098886	0.00029896	1.198

Figure 3·14: Numerical result of Geant4 simulation of Energy deposition.

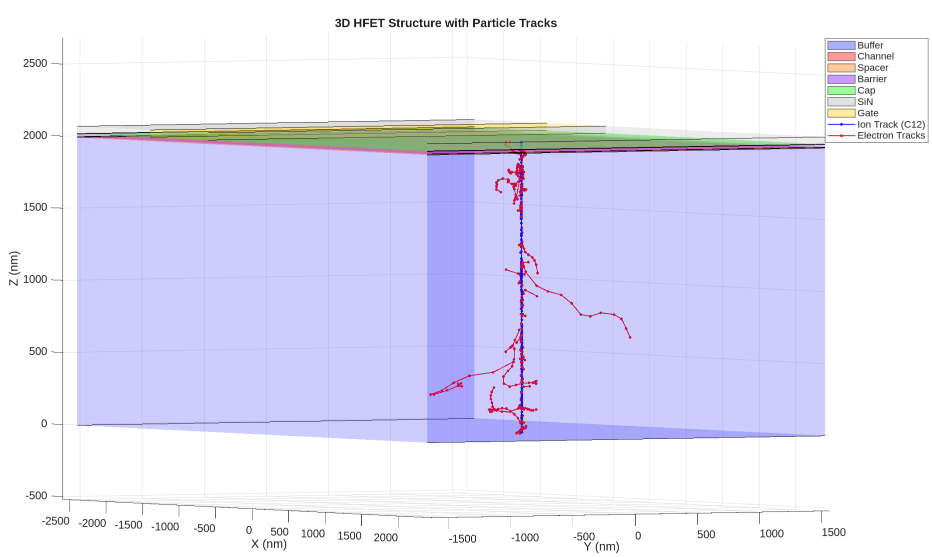

Figure 3·15: 3D energy deposition profile in HFET.

3.4 Summary of Geant4 Simulation

In general, two major simulations are conducted using Geant4: radiation energy deposition in materials and in devices.

From the material simulations, the ion–material interaction behavior can be summarized as follows: 1. Faster and lighter ions exhibit weaker interactions with the material and penetrate deeper. 2. Slower and heavier ions exhibit stronger interactions with the material and stop earlier. 3. Denser target materials also lead to stronger ion–material interactions and cause the incident ions to stop sooner. In addition, the accuracy of the results and the simulation code is validated against the reviewed SRIM data, where both the Bragg-peak magnitude and the independence of the Bragg-peak value with respect to penetration depth show good agreement.

From the device-structure simulation, describing the charge distribution simply as a dense track along the ion path is shown to be invalid when the device dimensions are comparable to the travel distance of delta electrons. To address this, a three-dimensional spatial energy-deposition profile is constructed in MATLAB.

With all Geant4 simulations completed, the research can now proceed to the next stage of the framework.

Chapter 4

TCAD Sentaurus Device Simulation of Irradiated HFET

After completing the energy-deposition simulation in the device structure and obtaining a three-dimensional spatial energy-deposition profile, a method is needed to perform device-level simulations to evaluate how the deposited energy affects device operation in the next stage of the methodology development.

The simulation tool used for this purpose is TCAD Sentaurus. In this chapter, I will demonstrate the process of completing the framework by incorporating the Geant4 simulation results into TCAD Sentaurus , along with the device-level simulation results obtained from this methodology.

4.1 Mapping Geant4 Result to Sentaurus

TCAD Sentaurus is well known for its ability to simulate carrier transport in semiconductor devices. However, directly implementing the raw energy deposition profile from Geant4 into TCAD Sentaurus is not feasible, because Sentaurus cannot accept energy deposition data directly. In this section, I will present all the steps involved in transforming the Geant4 output and incorporating it into the TCAD Sentaurus device simulation, as well as explain why each step is necessary.

4.1.1 Converting Deposited Energy to Electron-hole Pair

To successfully import the Geant4 simulation results into the Sentaurus device simulation, the energy deposited by the carbon ion and the generated delta electrons must be converted into the corresponding number of electron–hole pairs. To achieve this, the energy required to create an electron–hole pair in a semiconductor, proposed by R. C. Alig and S. Bloom, (Alig & Bloom, 1975)

$$E_{ehp} = 2.73E_g + 0.55$$

is used to divide the deposited energy, yielding the corresponding number of generated electron–hole pairs. For example, GaN, which has a bandgap of $E_g = 3.4\,\mathrm{eV}$, has an electron–hole pair creation energy of approximately $E_{ehp} \approx 9.8\,\mathrm{eV}$. Therefore, a deposited energy of 980 eV would generate about 100 electron–hole pairs.

4.1.2 Building a Map of Carrier Generation Rate

After obtaining the number of electron–hole pairs and their spatial locations, this information is used to construct a map of the carrier generation rate, since Sentaurus requires charge-carrier input to be expressed as a generation rate rather than as discrete electron–hole pairs at point-like coordinates. To achieve this, a certain number of electron–hole pairs are grouped together, and the generation density is calculated by dividing the total number of pairs in each group by the volume into which they are placed.

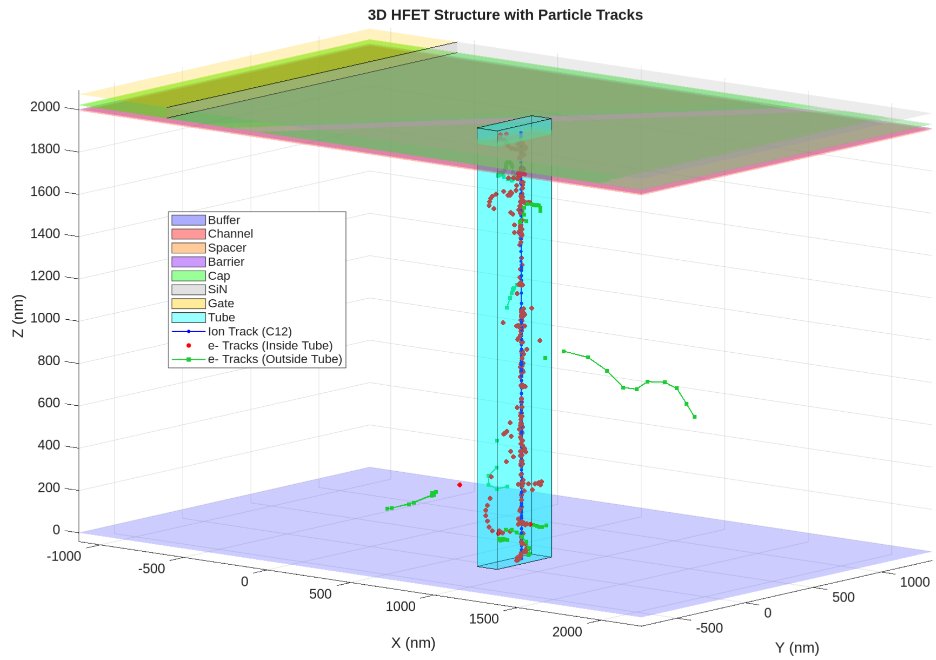

Figure 4·1: Charge grouping in HFET.

As shown in Figure 4.1, the main dense track of electron–hole pairs at $X = 3.8\,\mu$m is grouped into a tube with dimensions of 120 nm $\times$ 400 nm $\times$ 2000 nm tube. The corresponding generation density in this region is calculated by dividing the total number of electron–hole pairs (129,999 pairs in this case) by the volume of the tube ($9.6 \times 10^{-14}\,\text{cm}^3$). This yields a generation density of approximately $1.35 \times 10^{18}\,\text{cm}^{-3}$. The generation density is then divided by 0.1 picoseconds (1×10^{-13} s) to obtain a generation rate of $1.35 \times 10^{31}\,\text{cm}^{-3}\,t^{-1}$ for that region.

4.1.3 Sentaurus Device Simulation Setup

The setup of the Sentaurus device simulation is adapted from an example provided in the Sentaurus Application Library – HFET_GaN_DC – with modifications made to address radiation-effect analysis.

Device Structure

The device is constructed based on the provided Sentaurus example, and modified to have an additional region as shown in Figure 4.2.

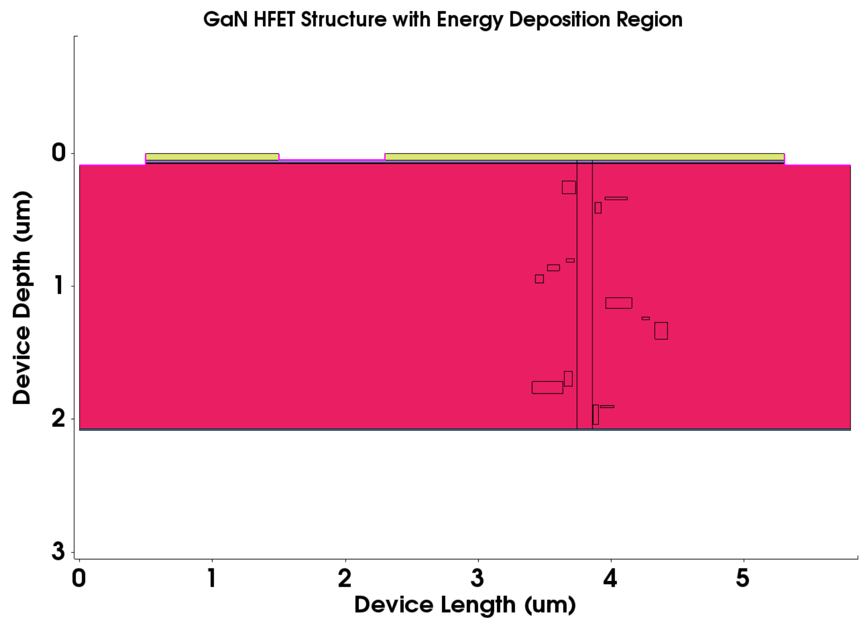

Figure 4·2: GaN HFET structure that has an indication of the energy deposition region.

As mentioned in the calculation of the generation rate, deposition events are grouped to calculate the corresponding charge-carrier generation rate. **The additional region shown in Figure 4.2 indicates the location where a generation rate is applied.** These regions are constructed based on the size and position of each grouping. For example, the main dense track of electron–hole pairs at $X = 3.8\mu$m, with dimensions of 120 nm $\times$ 400 nm $\times$ 2000 nm is mapped to the longest rectangular region at $X = 3.8\,\mu$m shown in Figure 4·2, which also has a length of 120 nm and a depth of 2000 nm.

Physics List

The physics list is modified from the Sentaurus example – HFET_GaN_DC, by adding additional models to address radiation-effect scenarios. These additional physics models include the avalanche model and optical generation. Enabling the avalanche model ensures that impact ionization caused by the heavy-ion strike is not neglected, while optical generation is used to implement the carrier generation rate.

Simulation Condition

For the final radiation-effect simulations on the HFET, all simulations are performed in transient mode to study how a heavy-ion strike influences the device's operational behavior. Each transient simulation is run from $t = 0$ to $t = 1\,\text{ns}$ under a fixed gate voltage of $-4\,\text{V}$, with the drain voltage set to one of four values: 75 V, 100 V, 125 V, or 150 V.

As mentioned in the calculation of the generation rate, each generation-rate entry has a value, a coordinate, and a duration. These quantities are set as simulation conditions and introduced into the Sentaurus simulation as a bias source applied at their corresponding spatial locations, with a constant generation value lasting for 0.1 ps from $t = 0.1\,\text{ps}$ to $t = 0.2\,\text{ps}$.

4.2 Sentaurus Simulation Result and Discussion

In this section, I will present the simulation results obtained from Sentaurus, including the device operation behavior without an ion strike and the device operation behavior after an ion strike.

4.2.1 Normal Operation Behavior

The normal operating behavior of the target device is investigated through a transient simulation using the previously discussed simulation conditions (see Sentaurus Simulation Condition), but without any optical-generation bias applied.

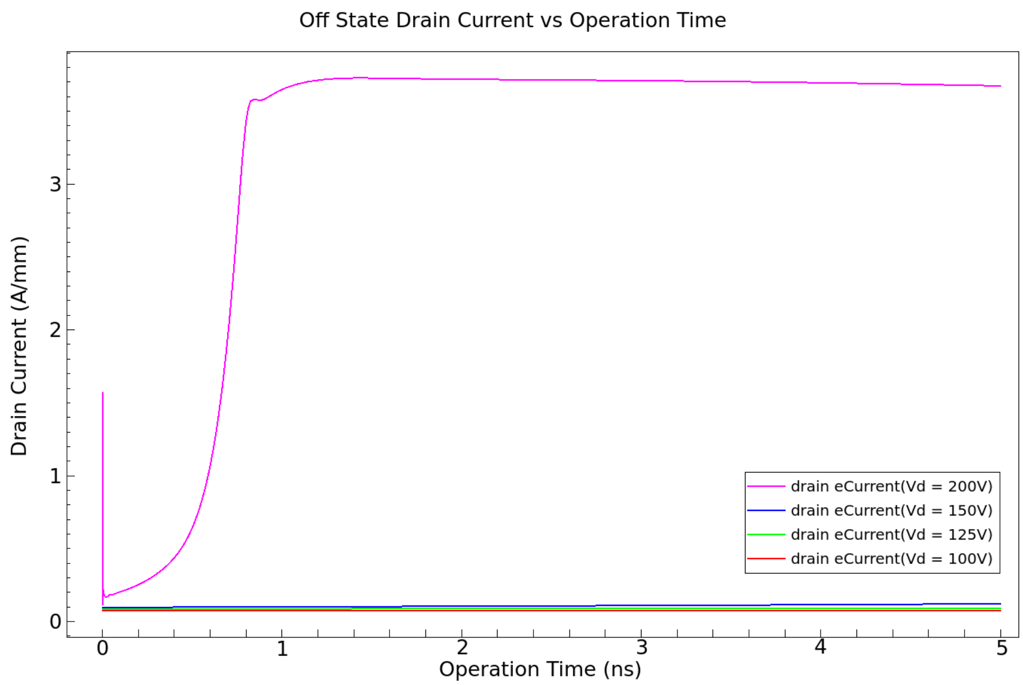

Figure 4·3: Target HFET operation behavior in off state.

As shown in Figure 4.3, the drain current remains small and nearly constant when the operating drain voltage is 100 V, 125 V, and 150 V. In contrast, the target HFET exhibits an operational threshold near 200 V, as indicated by the fact that the drain current no longer remains constant and increases dramatically around $t = 0.7\,\mathrm{ns}$.

4.2.2 Post-irradiation Operation Behavior

The operation behavior of the target device after the ion strike is investigated using the Sentaurus simulation setup discussed previously (see Sentaurus Simulation Condition).

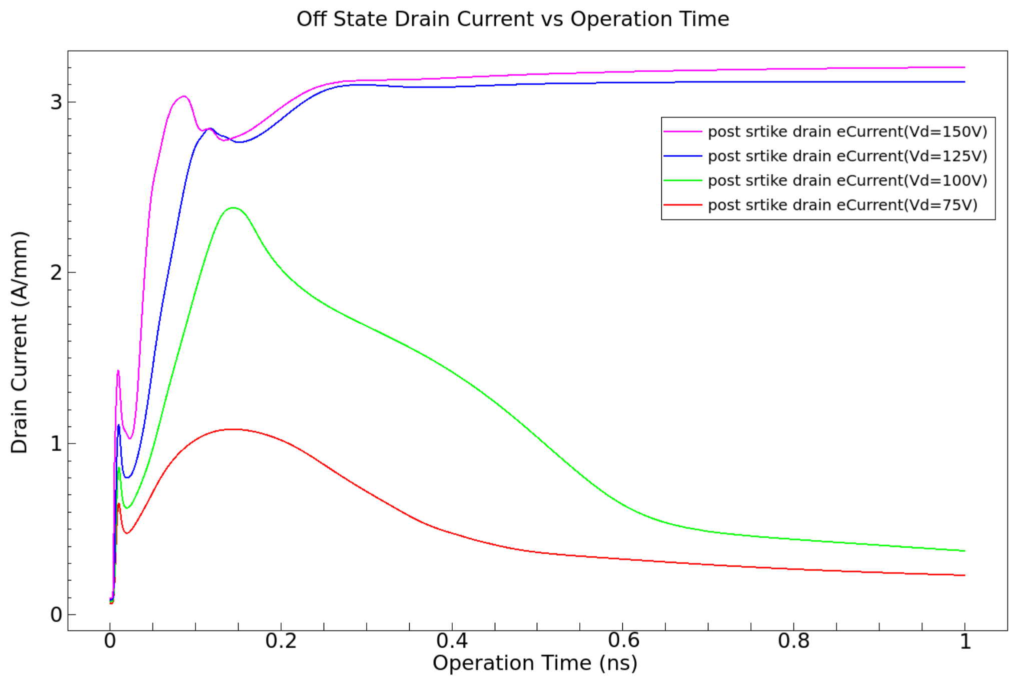

Figure 4·4: Target irradiated HFET operation behavior in off state.

As shown in Figure 4.4, compared to the unaffected HFET (Figure 4.3), the drain current exhibits abnormal behavior over time under the influence of the ion strike. Two peaks are observed in the plots, and for all four different operations, the drain voltage and drain current gradually increase between peaks. However, after the second peak, operation behavior differs depending on the operating voltage: at 75 V and 100 V, the drain current tends to return to its normal level, whereas at 125 V and 150 V, the drain current remains increased.

The phenomenon observed in Figure 4.4 reflects the underlying physics of single-event effects and carrier transport. In semiconductor carrier transport, electrons have much higher mobility than holes; therefore, electrons generated by ion strikes are collected by the drain first, producing the initial current peak. During the electron-collection process, the holes drift toward the gate under the influence of the electric field and begin to accumulate in the buffer layers beneath the gate region. This hole accumulation locally lowers the potential barrier between the source and drain, effectively creating a conduction path. As the hole concentration continues to increase, this path becomes more conductive, causing the drain current to rise gradually between the two peaks.

The collection and drift processes of the radiation-induced charge carriers are strongly influenced by the applied drain voltage; at higher drain voltages, these processes occur more intensively. As a result, for higher voltages such as 125 V and 150 V (as shown in Figure 4.4), more electrons are collected by the drain and more holes accumulate beneath the gate in a much shorter time, eventually causing impact ionization – reflected by the rise in drain current after the second peak (a single event burnout). In contrast, at lower voltages such as 100 V and 75 V, these processes occur more gradually, and the drain current eventually tends to return to its normal level (a single-event transient).

4.3 Summary of TCAD Sentaurus Simulation

The TCAD Sentaurus simulation reveals that an ion strike lowers the device's threshold operating voltage and demonstrates that single-event effects are strongly dependent on the applied operating voltage. More importantly, the drain-current-versus-time plots obtained in this research (Figure 4.4) show the same key features observed in other reviewed simulation results obtained using Sentaurus's built-in heavy-ion model (Figure 2.11) – specifically, the occurrence of two peaks in the drain current.

At last, the ability to obtain reasonable results demonstrates the successful implementation of the Geant4 output into TCAD Sentaurus and marks the completion of the methodology (framework) development.

Chapter 5

Conclusions and Future Work

In this thesis, a simulation framework was developed by integrating Geant4 and TCAD Sentaurus to study radiation effects in a high-electron-mobility field-effect transistor (HFET). Within this framework, Geant4—a Monte Carlo simulation toolkit—is employed to accurately model the spatial distribution of electron–hole pair generation induced by ion–material interactions, while TCAD Sentaurus is used to simulate the subsequent charge transport and device response.

During the development of the framework, Geant4 simulations of ion–material interactions show that the interaction intensity increases with the atomic number of the incident ion as well as with the properties of the target material. Furthermore, simulations of ion–device interactions reveal that representing the induced charge distribution as a simple dense track along the ion trajectory is insufficient. In addition to the primary ion track, energetic delta electrons are generated and can transport energy several micrometers away from the ion path, significantly enlarging the energy deposition region. When the characteristic dimensions of the device are comparable to the transport range of these delta electrons, their contribution cannot be neglected. Therefore, an accurate radiation-effect simulation must explicitly account for the trajectories of delta electrons to faithfully represent the energy deposition process.

TCAD Sentaurus simulations further demonstrate that the radiation response of the HFET is strongly dependent on the applied drain voltage, highlighting the importance of bias conditions in evaluating device susceptibility to radiation-induced effects.

In future work, the current two-dimensional Sentaurus simulations will be extended to three dimensions to achieve more realistic device modeling. In addition, the electron–hole pair grouping strategy will be further refined to explore the numerical and physical limits of Sentaurus. Finally, the mapping process between Geant4 and TCAD will be automated to improve the efficiency, scalability, and robustness of the overall simulation workflow.

Appendix A

Numerical expression of Density Effect

x is a kinetic variable of the particle : $x = \log_{10}(\gamma\beta) = \ln(\gamma^2\beta^2)/4.606$, and $\delta(x)$ is defined by

$$\begin{array}{lll} \text{for} & x < x_0: & \delta(x) = 0 \\ \text{for} & x \in [x_0,\ x_1]: & \delta(x) = 4.606x - C + a(x_1 - x)^m \\ \text{for} & x > x_1: & \delta(x) = 4.606x - C \end{array}$$

where the matter-dependent constants are calculated as follows:

$$\begin{aligned} h\nu_p &= \text{plasma energy of the medium } = \sqrt{4\pi n_{el} r_e^3} mc^2/\alpha = \sqrt{4\pi n_{el} r_e} \hbar c \\ C &= 1 + 2\ln(I/h\nu_p) \\ x_a &= C/4.606 \\ a &= 4.606(x_a - x_0)/(x_1 - x_0)^m \\ m &= 3. \end{aligned}$$

For condensed media

$$\begin{array}{ll} I < 100 \text{ eV} & \begin{cases} \text{for } C \leq 3.681 & x_0 = 0.2 & x_1 = 2 \\ \text{for } C > 3.681 & x_0 = 0.326C - 1.0 & x_1 = 2 \end{cases} \\ I \geq 100 \text{ eV} & \begin{cases} \text{for } C \leq 5.215 & x_0 = 0.2 & x_1 = 3 \\ \text{for } C > 5.215 & x_0 = 0.326C - 1.5 & x_1 = 3 \end{cases} \end{array}$$

and for gaseous media

$$\begin{array}{llll} \text{for} & C < 10. & x_0 = 1.6 & x_1 = 4 \\ \text{for} & C \in [10.0,\ 10.5[& x_0 = 1.7 & x_1 = 4 \\ \text{for} & C \in [10.5,\ 11.0[& x_0 = 1.8 & x_1 = 4 \\ \text{for} & C \in [11.0,\ 11.5[& x_0 = 1.9 & x_1 = 4 \\ \text{for} & C \in [11.5,\ 12.25[& x_0 = 2. & x_1 = 4 \\ \text{for} & C \in [12.25,\ 13.804[& x_0 = 2. & x_1 = 5 \\ \text{for} & C \geq 13.804 & x_0 = 0.326C - 2.5 & x_1 = 5. \end{array}$$

Figure A·1: Density effect Formulation with material properties from *Geant4 11.3 Physical Manual* (CERN, 2024).

Where I is the mean excitation energy of the material.

Appendix B

Tabulated Function in Barkas Correction

		$\kappa(b,x)$	
x	$b=1.6$	$b=1.8$	$b=2.0$
0.115	0.1944	0.1331	0.095 11
0.165	0.2161	0.1478	0.1052
0.215	0.2363	0.1620	0.1153
0.265	0.2544	0.1754	0.1251
0.315	0.2706	0.1877	0.1343
0.365	0.2851	0.1990	0.1431
0.415	0.2980	0.2095	0.1513
0.465	0.3095	0.2191	0.1590
0.515	0.3198	0.2279	0.1662
0.565	0.3290	0.2360	0.1729
0.615	0.3373	0.2434	0.1793
0.665	0.3447	0.2503	0.1852
0.715	0.3514	0.2566	0.1908
0.765	0.3575	0.2625	0.1960
0.815	0.3629	0.2679	0.2009
0.865	0.3679	0.2729	0.2055
0.915	0.3724	0.2774	0.2099
0.965	0.3765	0.2818	0.2139
1.	0.3792	0.2846	0.2166
1.3	0.3967	0.3043	0.2361
1.7	0.4081	0.3201	0.2534
2	0.4123	0.3277	0.2626
3	0.4134	0.3389	0.2794
4	0.4064	0.3396	0.2854
5	0.3970	0.3364	0.2865
6	0.3871	0.3316	0.2853
7	0.3774	0.3260	0.2829
8	0.3682	0.3203	0.2798
9	0.3596	0.3146	0.2763
10	0.3514	0.3090	0.2727
13	0.3304	0.2938	0.2622
17	0.3072	0.2760	0.2489
20	0.2930	0.2647	0.2400
30	0.2578	0.2359	0.2166
40	0.2337	0.2154	0.1993
50	0.2157	0.1999	0.1859
60	0.2016	0.1876	0.1751
70	0.1901	0.1774	0.1661
80	0.1806	0.1689	0.1586
90	0.1724	0.1616	0.1520
100	0.1653	0.1553	0.1463

Figure B·1: Tabulated Function, F_A in Barkas Correction (Ashley et al., 1973).

References

Albadri, A., Schrimpf, R., Galloway, K., & Walker, D. (2006). Single event burnout in power diodes: Mechanisms and models. *Microelectronics Reliability*, 46(2), 317–325. https://doi.org/https://doi.org/10.1016/j.microrel.2005.06.015

Alig, R. C. & Bloom, S. (1975). Electron-hole-pair creation energies in semiconductors. *Physical Review Letters*, 35, 1522–1525. https://doi.org/10.1103/PhysRevLett.35.1522

Arnould, M. & Goriely, S. (2003). The p-process of stellar nucleosynthesis: astrophysics and nuclear physics status. *Physics Reports*, 384(1), 1–84. https://doi.org/https://doi.org/10.1016/S0370-1573(03)00242-4

Ashley, J. C., Ritchie, R. H., & Brandt, W. (1973). Z_1^3-dependent stopping power and range contributions. *Physical Review. A*, 8, 2402–2408. https://doi.org/10.1103/PhysRevA.8.2402

Basaglia, T., Bell, Z. W., D'Agostino, D., Dressendorfer, P. V., Giani, S., Pia, M. G., & Saracco, P. (2024). Geant4: A game changer in high energy physics and related applicative fields. *Future Generation Computer Systems*, 159, 411–422. https://doi.org/https://doi.org/10.1016/j.future.2024.05.042

Berger, M. J., Inokuti, M., Andersen, H. H., Bichsel, H., Powers, D., Seltzer, S. M., Thwaites, D., & Watt, D. E. (1993). 2. electronic (collision) stopping powers from bethe's theory. *Reports of the International Commission on Radiation Units and Measurements*, os-25(2), 6–17. https://doi.org/10.1093/jicru_os25.2.6

Berger, M. J., Inokuti, M., Anderson, H. H., Bichsel, H., Dennis, J. A., Powers, D., Seltzer, S. M., & Turner, J. E. (1984). 6. density effect. *Reports of the International Commission on Radiation Units and Measurements*, os-19(2), 32–35. https://doi.org/10.1093/jicru_os19.2.32

CERN (2024). Geant4 physics reference manual. Technical report, Geant4 Collaboration. https://geant4.web.cern.ch. Version 11.3

Choudhury, A. K. R. (2014). 2 - object appearance and colour. *Principles of Colour and Appearance Measurement*, 53–102. Woodhead Publishing. https://doi.org/https://doi.org/10.1533/9780857099242.53

Cohen, C. M. S., Stone, E. C., Mewaldt, R. A., Leske, R. A., Cummings, A. C., Mason, G. M., Desai, M. I., von Rosenvinge, T. T., & Wiedenbeck, M. E. (2005). Heavy ion abundances and spectra from the large solar energetic particle events of October–November 2003. *Journal of Geophysical Research*, 110(A9). https://doi.org/https://doi.org/10.1029/2005JA011004

Coplan, M. A. (1995). *Solar wind composition : progress report*. NASA technical memorandum ; NASA TM-197364. Goddard Space Flight Center. https://ntrs.nasa.gov/api/citations/19950015967/downloads/19950015967.pdf

Cowan, J. J., Sneden, C., Lawler, J. E., Aprahamian, A., Wiescher, M., Langanke, K., Martínez-Pinedo, G., & Thielemann, F.-K. (2021). Origin of the heaviest elements: The rapid neutron-capture process. *Reviews of Modern Physics*, 93(1), 015002. https://doi.org/10.1103/RevModPhys.93.015002

Dimitrijev, S., Han, J., Haasmann, D., Moghadam, H. A., & Aminbeidokhti, A. (2014). Power-switching applications beyond silicon: The status and future prospects of SiC and GaN devices. *2014 29th International Conference on Microelectronics Proceedings - MIEL 2014*. https://doi.org/10.1109/MIEL.2014.6842083

Elert, G. (1998). *The physics hypertextbook*. https://physics.info/

FederalAviationAdministration (2016). *Single event effects mitigation techniques report*. https://rosap.ntl.bts.gov/view/dot/57661. [Accessed 28-08-2025]

He, X.-G., Zhao, D.-G., & Jiang, D.-S. (2015). Formation of two-dimensional electron gas at AlGaN/GaN heterostructure and the derivation of its sheet density expression. *Chinese Physics B*, 24(6), 067301. https://doi.org/10.1088/1674-1056/24/6/067301

ICRU (2005). 3 theory. *Journal of the ICRU*, 5(1), 21–67. https://doi.org/10.1093/jicru_ndi010

JuliaHEP Collaboration (2023). *Introduction to Geant4.jl*. https://juliahep.github.io/Geant4.jl/dev/. Julia bindings for the Geant4 particle transportation toolkit. Accessed: 2025-08-29

Karaağaç, M. O., Ergün, A., Arslan, O., & Kayfeci, M. (2023). Chapter 23 - introduction to solar panels. *Handbook of Thermal Management Systems*, 541–556. Elsevier. https://doi.org/https://doi.org/10.1016/B978-0-443-19017-9.00011-8

Kittel, C. (2004). *Introduction to solid state physics* (8 ed.). John Wiley & Sons.

Kutner, M. L. (2003). Preface. *Astronomy: A Physical Perspective*, xvii–xviii. https://doi.org/10.1017/CBO9780511802195

Käppeler, F. (1999). The origin of the heavy elements: The s process. *Progress in Particle and Nuclear Physics*, 43, 419–483. https://doi.org/https://doi.org/10.1016/S0146-6410(99)00098-8

Li, J., Wang, Y., Fei, X.-X., Sun, B., Song, Y.-X., & Bao, M.-T. (2025). TCAD analysis of single-event burnout caused by heavy ions for a GaN HEMT. *Journal of Computational Electronics*, 24(1). https://doi.org/10.1007/s10825-024-02275-1

Lindhard, J. & Sørensen, A. H. (1996). Relativistic theory of stopping for heavy ions. *Physical Review. A*, 53, 2443–2456. https://doi.org/10.1103/PhysRevA.53.2443

Loore, C. W. H. d. & Doom, C. (1992). *Structure and evolution of single and binary stars*. Astrophysics and space science library ; v. 179. Kluwer Academic Publishers. https://doi.org/10.1007/978-94-011-2502-4

Lv, Y., Chen, P., Foo, J., Zhang, J., Qian, W., Chen, C., & Ong, W.-J. (2022). Dimensionality-dependent mos2 toward efficient photocatalytic hydrogen evolution: from synthesis to modifications in doping, surface and heterojunction engineering. *Materials Today Nano*, 18, 100191. https://doi.org/https://doi.org/10.1016/j.mtnano.2022.100191

Meyer, B. S., Nittler, L. R., Nguyen, A. N., & Messenger, S. (2008). Nucleosynthesis and chemical evolution of oxygen. *Reviews in Mineralogy and Geochemistry*, 68(1), 31–53. https://doi.org/10.2138/rmg.2008.68.4

Naito, M. & Kodaira, S. (2022). Considerations for practical dose equivalent assessment of space radiation and exposure risk reduction in deep space. *Scientific Reports.*, 12(1), 13617. https://doi.org/10.1038/s41598-022-17079-1

NASA (2012). *NASA space faring*. Bibliogov. https://www.nasa.gov/wp-content/uploads/2017/04/radiationchallenge.pdf

Quadros de Aguiar, Y., Wrobel, F., Autran, J.-L., & García Alía, R. (2024). *Single-event effects, from space to accelerator environments* (2025 ed.). Springer International Publishing. https://doi.org/10.1007/978-3-031-71723-9

Rodríguez, T. (2014). Theoretical nuclear structure and astrophysics at fair. *Journal of Physics: Conference Series*, 503, 012038. https://doi.org/10.1088/1742-6596/503/1/012038

S. Agostinelli, e. a. (2003). Geant4—a simulation toolkit. *Nuclear Instruments and Methods in Physics Research Section A: Accelerators, Spectrometers, Detectors and Associated Equipment*, 506(3), 250–303. https://doi.org/https://doi.org/10.1016/S0168-9002(03)01368-8

Salpeter, E. E. (1957). Nuclear reactions in stars. buildup from helium. *Physical Review*, 107, 516–525. https://doi.org/10.1103/PhysRev.107.516

Sand, A. E., Ullah, R., & Correa, A. A. (2019). Heavy ion ranges from first-principles electron dynamics. *npj Computational Materials*, 5(1). https://doi.org/10.1038/s41524-019-0180-5

Sigmund, P. (2006). *Dielectric Stopping Theory*, 141–180. Springer Berlin Heidelberg. https://doi.org/10.1007/3-540-31718-X_5

Sigmund, P. & Schinner, A. (2014). Notes on barkas-andersen effect. *European Physical Journal. D, Atomic, Molecular, and Optical Physics*, 68(10).

Sigmund, P. & Schinner, A. (2020). The bloch correction, key to heavy-ion stopping. *Journal of Applied Physics*, 128(10), 100903. https://doi.org/10.1063/5.0015478

Sternheimer, R. M. & Peierls, R. F. (1971). General expression for the density effect for the ionization loss of charged particles. *Physical Review. B*, 3, 3681–3692. https://doi.org/10.1103/PhysRevB.3.3681

Whitman, K., Norbury, J. W., Lee, K., Slaba, T. C., & Badavi, F. F. (2019). Comparison of space radiation GCR models to AMS heavy ion data. *Life Sciences in Space Research*, 22, 76–88. https://doi.org/10.1016/j.lssr.2019.07.007

Wiescher, M. (2018). The history and impact of the CNO cycles in nuclear astrophysics. *Physics in Perspective*, 20(1), 124–158. https://ui.adsabs.harvard.edu/abs/2018PhP....20..124W/abstract

Wright, E. L. (Sep 26, 2012). *Big bang nucleosynthesis*. https://astro.ucla.edu/~wright/BBNS.html

Yin, X. (2014). *Introduction to the geant4*. https://indico.ihep.ac.cn/event/4287/contributions/65981/attachments/33185/38536/Intorduction_to_the_Geant4.pdf. Lecture slides

Zhang, J., Guo, J., Zhang, Y., Cao, Y.and Dobynde, M. I., & Li, C. e. a. (2024a). The 2022 february 15 solar energetic particle event at mars: A synergistic study combining multiple radiation detectors on the surface and in orbit of mars with models. *Geophysical Research Letters*, 51(19), e2024GL111775. https://doi.org/https://doi.org/10.1029/2024GL111775

Zhang, X., Cao, Y., Chen, C., Wu, L., Wang, Z., Su, S., Zhang, W., Lv, L., Zheng, X., Tian, W., Ma, X., & Hao, Y. (2024b). Study on single event effects of enhanced GaN HEMT devices under various conditions. *Micromachines (Basel)*, 15(8). https://doi.org/10.3390/mi15080950

CURRICULUM VITAE

[redacted]